The anharmonic infrared spectra of polycyclic aromatic hydrocarbons

Mackie, J.C.

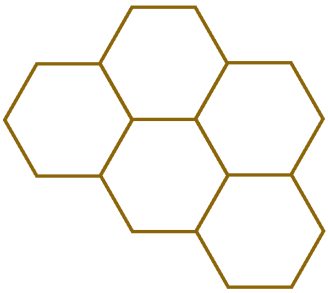

The anharmonic quartic force field infrared spectra of hydrogenated and methylated PAHs

Polycyclic aromatic hydrocarbons (PAHs) have been shown to be ubiquitous in a large variety of distinct astrophysical environments and are therefore of great interest to astronomers. The majority of these findings are based on theoretically predicted spectra, which make use of scaled DFT harmonic frequencies for band positions and the double harmonic approximation for intensities. However, these approximations have been shown to fail at predicting high–resolution gas–phase infrared spectra accurately, especially in the CH–stretching region (2950–3150 cm^{-1}, 3μm). This is particularly worrying for the subset of hydrogenated or methylated PAHs of which astronomers attribute the observed non–aromatic features which appear in the CH–stretching region of spectral observations of the interstellar medium (ISM). In our previous works, we presented the anharmonic theoretical spectra of three linear PAHs and five non–linear PAHs, demonstrating the importance of including anharmonicities into theoretical calculations. In this work we extend these techniques to two methylated PAHs (9–methylanthracene, and 9,10–dimethylanthracene) and four hydrogenated PAHs (9,10–dihydroanthracene, 9,10–dihydrophenanthrene, 1,2,3,4–tetrahydronaphthalene, and 1,2,3,6,7,8–hexahydro–pyrene) in order to better understand the aliphatic IR features of substituted PAHs. The theoretical spectra are compared with spectra obtained under matrix isolation low–temperature conditions for the full vibrational fundamental range and high–resolution, low–temperature gas-phase conditions for the CH–stretching region. Excellent agreement is observed between the theoretical and high–resolution experimental spectra with a deviation of 0.00% ±0.17%, and changes to the spectra of PAHs upon methylation and hydrogenated are tracked accurately and explained.

C. J. Mackie, A. Candian, X. Huang, E. Maltseva, A. Petrignani, J. Oomens, W. J. Buma, T. J. Lee, and A. G. G. M. Tielens, Phys. Chem. Chem. Phys. **20**, 1189 (2018)

5.1 Introduction

Due to their remarkable stability, Polycyclic Aromatic Hydrocarbon (PAH) molecules are widespread in everyday life. They are a major component of soot, created during combustion processes[114] and their biological activity makes them pollutants of water and the atmosphere. In the terrestrial atmosphere, several reactions[115] lead to functionalised PAHs - PAHs with chemical side groups and/or heteroatom substitution. These functionalisations have an impact on the properties of the molecules, for example methylation can increase or decrease the carcinogenicity level of PAHs depending on the substitution position[116].

Functionalised PAHs are also of interest from a material science prospective. For example, hydrogenationation of PAHs change the local molecule hybridization from sp^2 to sp^3, and are therefore a model system for studies of hydrogenated graphene, which are promising successors of silicon in the electronic industry thanks to the tunability of the graphene band gap depending on the location of additional hydrogens[8].

Several studies indicate that PAHs are also of high importance in astrophysical environments. PAHs have been detected in interplanetary dust particles and meteorites[14, 117], and are most certainly the carriers of the Aromatic Infrared Bands (AIBs)[29, 30], a family of IR emission features spanning the 3-20 μm (3300-500 cm^{-1}) region, seen in a variety of astrophysical environments. In particular, hydrogenated and methylated PAHs are considered to be responsible for additional features at 3.40, 3.46, 3.51, 3.56 μm and 6.9 μm[39, 40, 41, 118, 119], which can be particularly strong in evolved stars[120]. Also, hydrogenated PAHs have gained interests as potential catalysts for H_2 formation in astrophysical regions dominated by visible-ultraviolet photons[121].

IR spectra of methylated and hydrogenated PAHs have been explored both experimentally[122, 123], mostly in a matrix-environment[124], and computationally using DFT and the double harmonic approximation [85]. For normal PAHs, previous experiments have shown that the theoretical double harmonic spectra compare poorly, especially in the 3.1-3.5 μm (3200-2900 cm^{-1})[25], and 5-6 μm (2000-1600 cm^{-1}) regions[105]. This is due to the inability of the harmonic approximation to account for combination bands, overtones, mode couplings and resonances.

In our previous work[25, 26, 105, 125] we showed that good agreement between theoretical and experimental spectra can be obtained when an anharmonic theoretical approach is used; specifically a second–order vibrational perturbation treatment, that accounts for large numbers of mutually resonating modes and combination bands. This work expands upon these studies in order to address the high–resolution spectra of hydrogenated and methylated PAHs. The anharmonic treatment is applied to six "decorated" PAH species: 9–methylanthracene, 9,10–dimethylanthracene, 9,10–dihydroanthracene, 9,10–dihydrophenanthrene, 1,2,3,4–tetrahydronaphthalene, and 1,2,3,6,7,8–hexahydropyrene (see figure 5.1). The goal is two–fold: to further expand and test the anharmonic methods outlined in our previous works to include hydrogenated and methylated species, and to explain how and why PAH spectra change with the introduction of aliphatic groups. A

robust theoretical understanding of the IR spectral features and the role of anharmonicities is key to analyzing and interpreting astronomical observations. Important particularly with the upcoming launch of the James Webb Space Telescope in 2018, as astronomers will get for the first time astronomical spectra at high spectral resolution and high sensitivity.

Of particular interest is the behavior of aliphatic vibrational modes in resonances with the CH–stretching region around 3 μm. For this we compare low–temperature high–resolution gas–phase IR absorption spectra of the six decorated species which allows direct comparisons to the theoretical methods, further validating our approach. Full peak analyses are given for the bands in the CH–stretching region. The remaining IR range is also compared to the available matrix isolation spectra (MIS) and high–temperature gas–phase spectra to confirm accuracy in the full IR range.

5.2 Theoretical Methods

The theoretical methods of this work follow similar techniques of our previous work[97, 105, 125]. The software package Gaussian09[53] is used to optimize the geometry of the molecules, as well as to calculate the quartic force fields (QFFs) and IR intensities. In order to handle the large number of mutually resonating modes (*polyads*[58]) we use a locally modified version of the SPECTRO[54] software package to perform a second order vibrational perturbation theory treatment (VPT2) after transforming the QFF constants from normal to Cartesian coordinates[97]. We use the resulting eigenvalues of the VPT2 polyad treatment for the final line positions and the square of the eigenvectors to distribute intensities over resonating modes (see ref. [105, 125] for more details).

Recently, problems with the stability of the quartic force field of PAHs using the B97-1 functional[93] and TZ2P basis set[94] combination has been discovered. Therefore, a switch has been made in this work to the B3LYP hybrid functional[126, 127], and the polarized double-ζ basis set N07D[128], a combination developed specifically for the anharmonic calculations of medium-size molecules in mind[52].

Known issues arise in the anharmonic analysis involving the low barrier "free–rotor" vibrational modes of methyl groups[129]. To circumvent this issue, cubic and quartic force constant terms involving the free–rotor modes were set to zero, essentially treating these vibrational modes at the harmonic level.

5.3 Results

Comparisons between the theoretical anharmonic spectra and experimental spectra obtained under the two experimental conditions were performed. To aid in the comparisons, the theoretical spectra have been convolved[130] with Lorentzian profiles to best match the experimental band–widths. Band assignments are made between theory and experiment based on position, intensity, and local trends of

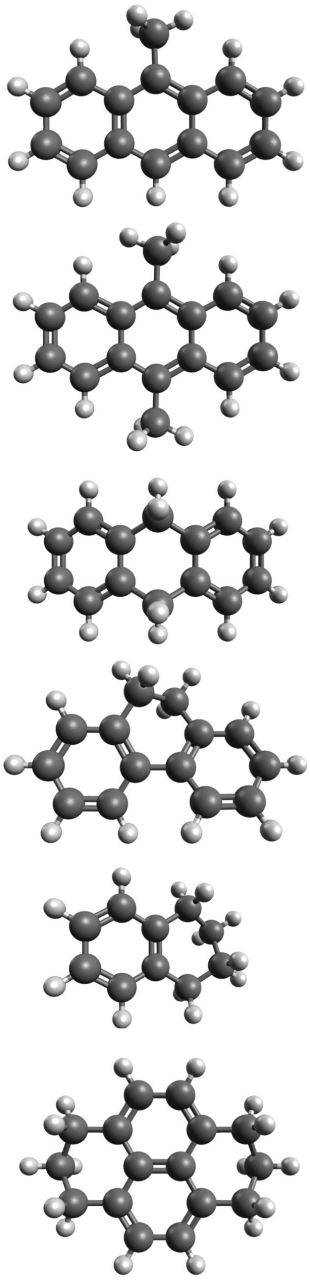

Figure 5.1 From top to bottom: 9–methylanthracene, 9,10–dimethylanthracene, 9,10–dihydroanthracene, 9,10–dihydrophenanthrene, 1,2,3,4–tetrahydronaphthalene, and 1,2,3,6,7,8–hexahydropyrene. Symmetries from top to bottom: C_s, C_{2h}, C_2, C_2, C_2, C_{2v}

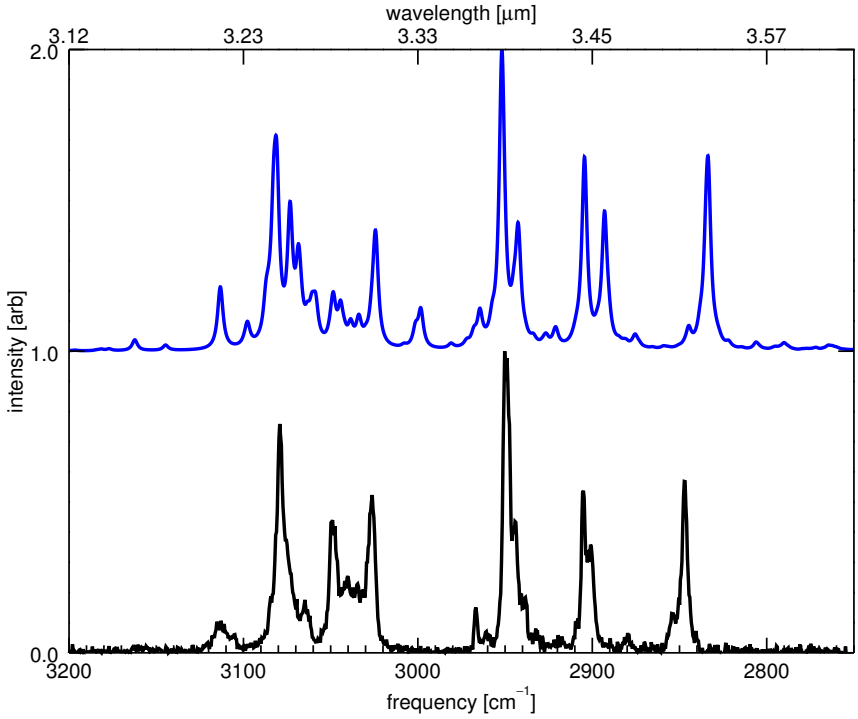

Figure 5.2 Theoretical anharmonic IR spectrum of this work of 9,10–dihydrophenanthrene compared with the high–resolution gas–phase IR absorption spectrum of this work.

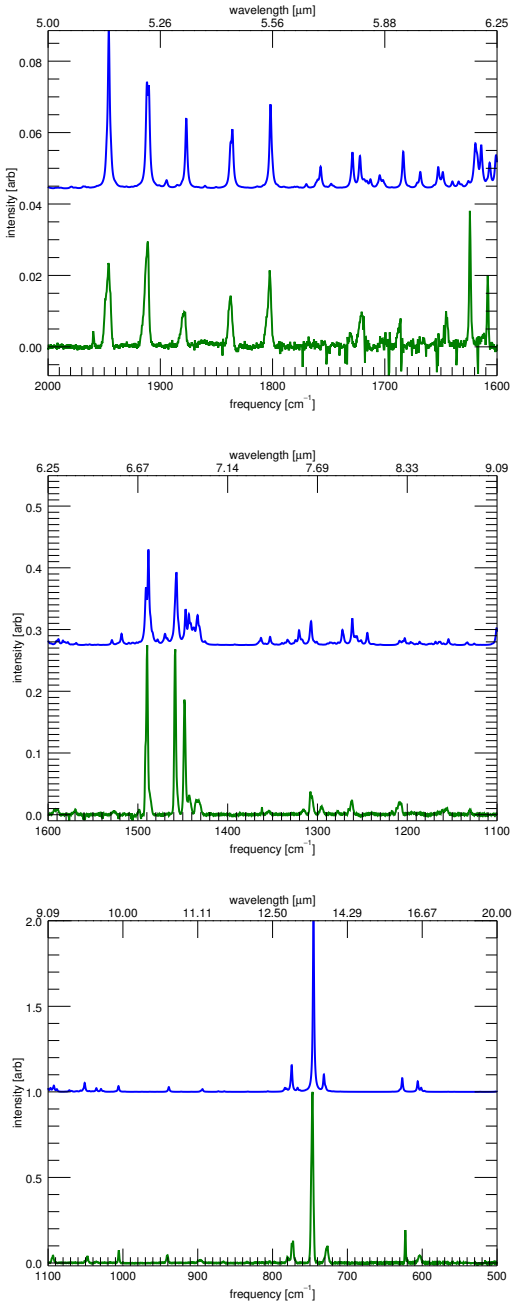

Figure 5.3 The matrix–isolation infrared spectrum[36, 79] of 9,10-dihydrophenanthrene (green, bottom of each panel) compared to the convolved (FWHM 2 cm^{-1}) theoretical anharmonic calculations of this work (blue, top each panel). Three spectral ranges are shown.

the convolved spectra. The values given for the experiment and theory are obtained through fitting Lorentzian profiles using the software package Fityk[110]. Vibrational mode descriptions were obtained through visualization of the atomic motions of each of the normal modes.

Figure 5.14 shows an example comparison between the convolved theoretical spectra (blue, HWHM = 1.6 cm^{-1}) and the high–resolution low–temperature gas–phase spectra (black), both normalized to their highest peak in this spectral range. See ESI for similar comparisons for the remaining molecules. Detailed band assignments are also given in the ESI for each PAH. Due to strong resonances in the CH–stretching region assignment to a single unique fundamental or combination bands is not possible; instead the dominant resonant components (typically over 10% contribution) are given. Intensity source is given as a separate column since a small resonance component (< 10%) can be the dominant source of intensity if the related fundamental is very intense (see Theory section of reference 105 for more details). Vibrational mode descriptions are also given for each PAH in corresponding tables (see ESI).

High–resolution low–temperature gas–phase experimental data does not exist for the full infrared range, so comparisons are performed between the anharmonic spectra and the available MIS[124, 131] spectra for the remaining IR range. Figure 5.15 shows an example comparison between the convolved theoretical spectra (blue, HWHM = 1 cm^{-1}) and the MIS spectra (green). See ESI for similar comparisons for the remaining molecules. Three ranges are shown for each molecule, 2000–1600 cm^{-1}, 1600–1100 cm^{-1}, and 1100–500 cm^{-1}. No significant features appear between 3000 and 2000 cm^{-1}. No data is available below 500 cm^{-1}. All intensities, both theoretical and experimental, are scaled to the their maximum intensity in the spectral range (2000–500 cm^{-1}). Assignments between the MIS data and the anharmonic data of this work is also presented in the ESI.

When changing from B97-1/TZ2P to B3LYP/N07D the improvement in agreement to between theory and experiment was found to be significant; from an error of 1% down to 0.1% (30 cm^{-1} to 3 cm^{-1} in the CH–stretching region). Further functional/basis set benchmark studies on the anharmonic spectra of PAHs is warranted and currently underway.

5.4 Discussion

5.4.1 Overall comparison to the low–temperature high–resolution gas–phase spectra

The low–temperature high–resolution gas–phase spectra and the corresponding convolved theoretical spectra (see ESI) show excellent agreement. Figure 5.4 shows a histogram of the percent differences between the theoretical and experimental line positions for the six PAHs combined. A fitted Gaussian gives an average deviation of 0.00% ± 0.17%. For *all* of the theoretical spectra in the CH–stretching region there appears to be a systematic shift of of the lowest energy aliphatic modes. This accounts for the secondary bump centered around -0.6% in the histogram of figure 5.4. The push to lower energies indicates an overcorrection of the anharmonic

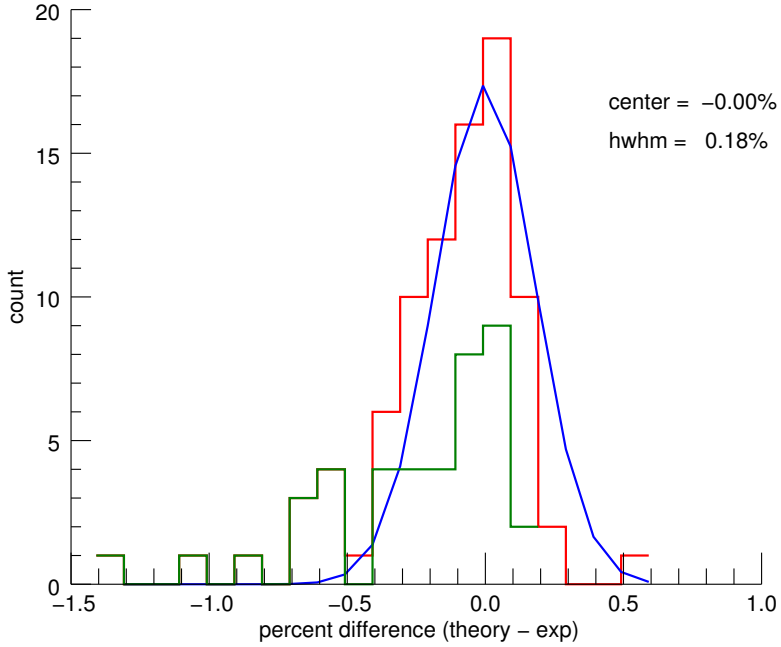

Figure 5.4 Histogram showing the percent differences between the line positions of the anharmonic theory (this work) and the low–temperature high–resolution gas–phase experiments for all six PAH species combined.

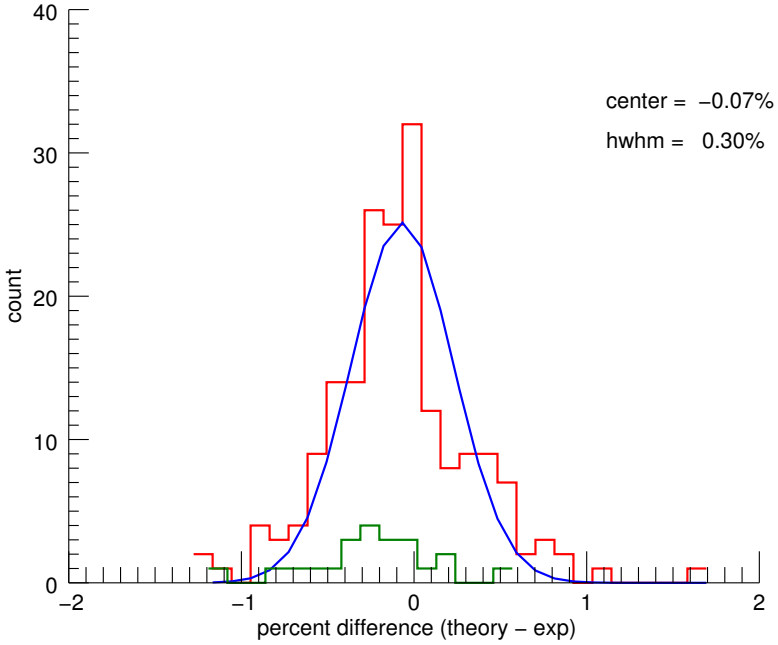

Figure 5.5 Histogram showing the percent differences between the line positions of the anharmonic theory (this work) and the MIS experiments for the five (no MIS data exists or 9,10–dimethylanthracene) PAH species combined.

effects. Whether this is due to the anharmonic correction of the bands, or due to the resonance terms themselves is not clear. The freezing of the methyl rotors could also be a factor, however the appearance of the same shift in the hydrogenated PAHs points away from this explanation. Future benchmark studies, including the decorated PAHs can address this minor issue.

Relative intensity agreement is moderate with an average deviation of -12% ± 50%. The major source of error in calculating the intensities of the CH–stretching region is the reliance on the distribution of harmonic intensities through the polyads rather than anharmonic intensities[105, 125]. Calculation and redistribution of "true" anharmonic intensities should improve the fits. The discrepancies between the theoretical and experimental intensities did not hamper reliable band identifications.

5.4.2 Overall comparison to MIS

The MIS spectra and the corresponding convolved theoretical spectra (see ESI) show good agreement. Figure 5.5 shows a histogram of the percent differences between the theoretical and experimental line positions for five of the PAHs combined (no MIS data exists for 9,10–dimethylanthracene). A fitted Gaussian gives an average deviation of -0.07% ± 0.30%. Previous work[111] has shown the unpredictable shifts due to matrix interactions to be 0.21% ± 0.63%. Therefore the theoretical spectra are accurate to within the limitations of MIS spectroscopy.

Relative intensity agreement is moderate with an average deviation of -18% ± 62%. It was possible to make use of anharmonic intensities in this region, however MIS experiments are notorious for affecting the intensities of bands. Therefore, confirmation of the reliability of the anharmonic intensity calculations needs to await high–resolution low–temperature gas–phase spectra in this region.

5.4.3 Anthracene series

Three anthracene–based PAHs have been considered: 9–methylanthracene; 9,10–dimethylanthracene; and 9,10–dihydroanthracene. Figure 5.6 shows the theoretical IR spectra of these three molecules in comparison with the theoretical spectrum of anthracene. Absolute intensities have been doubled, with the main peaks truncated, to show detail of the smaller peaks.

The most prominent change when moving from anthracene to the methylated and hydrogenated versions occurs in the CH–stretching region, with both methylated species bearing a strong resemblance to one another and to a lesser extent with the hydrogenated version. While anthracene shows one dominant peak, the decorated PAHs show five prominent features. These five features can be split into three regions based on the vibrational modes involved in the Fermi resonances:

1) Combinational aromatic states of CC–stretching modes paired with CH–in–plane–bending modes in Fermi resonances with aromatic CH–stretching modes. The behavior of this region is comparable to the "regular" CH–stretching region of a typical PAH. In anthracene this produces one main feature centered around 3055 cm^{-1}, while for the decorated anthracenes this feature is centered around 3085

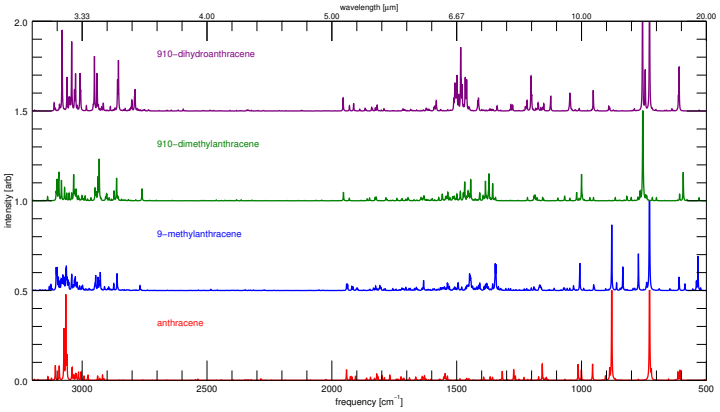

Figure 5.6 Comparison between anthracene–containing PAHs from the anharmonic theoretical spectra.

cm^{-1}. The push to higher energies is likely reflects steric interactions between the native anthracene hydrogens and the additional hydrogens. For the methylated anthracenes this region spans approximately 30 cm^{-1}, while the hydrogenated anthracene spans approximately 60 cm^{-1}. In regular anthracene this region spans the whole CH–stretching region (approximately 200 cm^{-1}).

2) Combinational aromatic/aliphatic states of CC–stretching modes paired with CH–in–plane–bending modes in Fermi resonances with aliphatic CH–stretching modes. For the methylated anthracenes this region is centered around 3055 cm^{-1} with a width of 30 cm^{-1} and is characterized by one dominant peak, while the hydrogenated anthracene is centered around 2960 cm^{-1} with a width of 160 cm^{-1} and is characterized by two dominant peaks.

3) Combinational aliphatic states of CH–in–plane–bending modes paired with CH–in–plane–bending modes in Fermi resonances with aliphatic CH–stretching modes. For the methylated anthracenes this region is centered around 2960 cm^{-1} with a width of 150 cm^{-1} and is characterized by two dominant peaks, while the hydrogenated anthracene is centered around 2849 cm^{-1} with a width of 50 cm^{-1} and is again characterized by two dominant peaks. The additional feature observed in the theoretical spectra of both methylated anthracenes around 2760 cm^{-1} are not observed in the experimental spectra.

One could argue that the region between 1000 and 600 cm^{-1} shows more variation between the anthracene–like species than the CH–stretching region around 3000 cm^{-1}. However, this is misleading. The differences are not directly due to methylation and hydrogenation, but rather indirectly due to the disruption of the types of CH bonds present in the molecule. As has been shown previously[33], the position of the bands in this region is sensitive to the the number of hydrogen atoms on a given aromatic ring involved in out–of–plane CH–bending modes.

For example, anthracene has two features in this region: one at 885 cm^{-1} from the out–of–plane CH–bendings of the hydrogens on the middle ring, or *solo* hydrogens (no adjacent hydrogens); and one at 730 cm^{-1} from the out–of–plane CH–bendings of the hydrogens on the terminal rings, or *quarto* hydrogens (four adjacent hydrogens). Similar characteristic features exist at distinct frequencies for other aromatic ring types; *duo* (two adjacent hydrogens) out–of–plane CH–bendings and *trio* (three adjacent hydrogens) out–of–plane CH–bendings. The intensity ratios of these bands have also been shown to correlate with the ratios of the edge structure of PAHs. Therefore, when moving from anthracene to 9–methylanthracene, the intensity of the solo CH–bending mode is observed to be reduced by a factor of two because one of the solo hydrogens has been replaced with the methyl group. This trend continues into 9,10–dimethylanthracene with the elimination of the solo CH–bending mode as both solo hydrogens have been replaced with methyl groups. Similarly, with 9,10–dihydroanthracene both solos are eliminated with the hydrogenation resulting in the loss of the solo CH–bending mode feature. Other subtle differences exist as well. When moving from anthracene to 9–methylanthracene to 9,10–dimethylanthracene two sets of bands appear and disappear around 840 cm^{-1} and 775 cm^{-1}. These bands are again due to solo and quarto hydrogen bending modes. The appearance and disappearance of these bands is likely due to symmetry effects. These modes are weak or inactive in the higher symmetric anthracene, gain considerable intensity with the breaking of symmetry from the addition of one methyl group, and lose intensity again with the near symmetry restoration from the addition of the second methyl group. The splitting of the quarto feature of 9,10–dihydroanthracene is due to interference from the hydrogenated groups.

The final region that shows significant change in the methylated and hydrogenated versions of anthracene is from 1600 to 1300 cm^{-1}. Intensity in this region is doubled or even tripled compared to normal anthracene. This region is dominated by out–of–plane combination bands including CH–bends paired with CH–bends, CH–bends paired with CC–bends, and CC–bends paired with CC–bends. The enhancement of this region is likely due to the disruption of the planarity of the molecules, leading to stronger dipoles for the out–of–plane combination bands.

5.4.4 Hydrogenated series

Four hydrogenated PAHs have been considered: 9,10–dihydroanthracene; 9,10–dihydrophenanthrene; 1,2,3,4–tetrahydronaphthalene; and 1,2,3,6,7,8–hexahydro–pyrene. Figure 5.7 shows the theoretical IR spectra of these four molecules in comparison with their non–hydrogenated counterparts from our previous work[25, 105]. Absolute intensities have been doubled, with the main peaks truncated, to show detail of the smaller peaks. 9,10–dihydroanthracene is absent from figure 5.7, see figure 5.6 for its comparison.

As stated previously, the most dramatic change to the spectra occurs in the CH–stretching region of the PAHs upon hydrogenation. The features centered around 3080 cm^{-1} of all four hydrogenated PAHs behave similar to their normal PAH counterparts in that they are aromatic CH–stretching modes in resonance

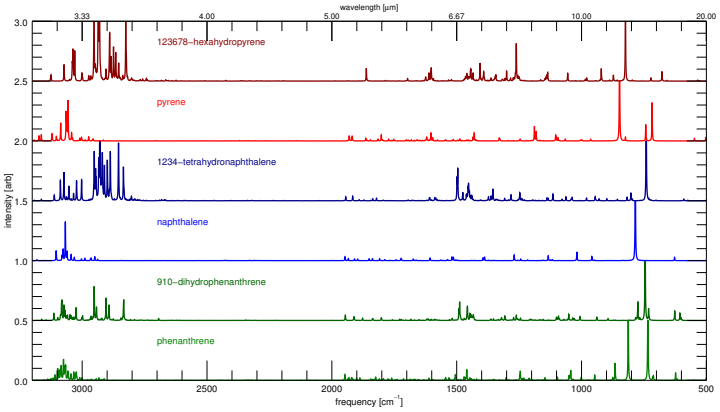

Figure 5.7 Comparison between normal and hydrogenated versions of PAHs from the anharmonic theoretical spectra.

with combination bands of CC–stretching with in–plane CH–bending modes. A spreading of intensity over a larger region is also observed in each of the hydro–PAHs when compared to their normal counterparts, especially for lower energy modes down to 3020 cm^{-1}. A break occurs before a sharp rise in aliphatic features beginning at 2950 cm^{-1} for all four hydro–PAHs. Three aliphatic regions then exist for each hydro–PAH: the features centered around 2950 cm^{-1} are due to in–plane CH–stretching modes of the aliphatic CH bonds that do not participate strongly in resonances; the features centered around 2900 cm^{-1} are due to out–of–plane CH–stretching modes of the aliphatic CH bonds in resonances; and the features centered near 2850 cm^{-1} are due to less sterically hindered out–of–plane CH–stretching modes of the aliphatic CH bonds in resonances. Notable changes can also be observed in the CH–stretching region as hydrogenation increases. In the slightly hydrogenated PAHs (9,10–dihydroanthracene and 9,10–dihydrophenanthrene) the aromatic region contains many closely spaced features, while the aliphatic region has fewer and more widely spaced features. In the highly hydrogenated PAHs (1,2,3,4–tetrahydronaphthalene and 1,2,3,6,7,8–hexahydropyrene) the opposite is true, the aliphatic region contains many closely spaced features, while the aromatic region has fewer and more widely spaced features. As shown in our previous work[105, 125], and confirmed here, the large number of closely spaced features in the CH–stretching region are due to strong Fermi resonances. As such there is not only the obvious loss of aromatic CH–stretching fundamentals and a gain in the aliphatic CH–stretching fundamentals as expected upon hydrogenation, but there is also a Fermi resonance shift from aromatic fundamentals and aromatic combination bands to between aliphatic fundamentals and aliphatic combination bands. This results in the forest of features moving from the aromatic region to the aliphatic region as observed in the highly

hydrogenated species.

As in the methyl–anthracene series significant changes occur in the 1000 and 600 cm^{-1} region. Again, these changes are not unique to hydrogenation, but rather reflect the loss of solo, duo, trio and quarto hydrogen edges. In 9,10–dihydroanthracene the solo CH–bending mode near 900 cm^{-1} is lost as both solo sites are hydrogenated. In 9,10–dihydrophenanthrene the duo CH–bending mode near 800 cm^{-1} is lost upon hydrogenation. In 1,2,3,4–tetrahydronaphthalene significant intensity is lost in the quarto CH–bending mode near 780 cm^{-1} as four out of eight quarto sites are hydrogenated, as well as a slight shift of the quarto bending mode to lower energy as the aromaticity is disrupted. In 1,2,3,6,7,8–hexahydropyrene the trio CH–bending modes near 780 cm^{-1} are lost as upon hydrogenation of the six trio hydrogens, as well as a slight shift of the duo bending mode to lower energy as the aromaticity is disrupted.

A significant increase in intensity is also observed in the bands near 1500 cm^{-1} for all of the hydrogenated PAHs. However, unlike the methylated species these features are more localized and are due to CH_2 bending modes of the hydrogenated sites.

5.4.5 Astrophysical implications

Determination of the carriers of the minor features observed at 3.40, 3.46, 3.51, and 3.56 μm (2941, 2890, 2849, and 2809 cm^{-1}) in the CH–stretching region of the AIBs is important to understanding the chemical populations in various physical environments. The lack of, or abundance of, these features in environments can point to chemical– or photo–processing of PAHs in space. It is generally believed that these bands are due to aliphatic substitutions to PAHs, either through hydrogenation or alkylation[39]. It has been shown previously[124] that the aliphatic groups of hydrogenated PAHs can indeed reproduce most of these features. Our work here confirms these findings. All four hydrogenated PAHs studied are able to contribute to the features observed at 3.40, 3.46, and 3.51 μm. For 9,10–dihydroanthracene and 9,10–dihydrophenanthrene the features are distinct and easily classified. The feature at 3.40 μm is due to in–plane CH–stretching modes of the hydrogenated sites with little contribution from resonances. The two features at 3.46, and 3.51 μm are due to out–of–plane CH–stretching modes of the hydrogenated sites in strong resonances with combination bands of paired CH–bending modes. The splitting of the out–of–plane CH–stretching modes into the two distinct features is due to the particular modes that are involved in the resonances. Moving up in the degree of hydrogenation with 1,2,3,4–tetrahydronaphthalene and 1,2,3,6,7,8–hexahydropyrene the previously distinct vibrational regions are now blurred into one. While both highly hydrogenated PAHs show many features centered near 3.40, 3.46, and 3.51 μm they are less separated in the spectra. This region is now dominated by Fermi resonances, resulting in many more aliphatic spectral features than seen for the dihydrogenated PAHs. This leads to the possibility that astronomical PAHs with only a few hydrogenated sites would show sharp distinct features around 3.40, 3.46, and 3.51 μm, while PAHs with a majority of hydrogenated sites would show wide blended features around 3.40, 3.46, and 3.51

μm. Although, the feature at 3.56 μm is unaccounted for in all of the theoretical spectra. The methylated PAHs 9–methylanthracene and 9,10–dimethylanthracene both show contributions to the 3.40, and 3.46 μm features. Here these features arise from the CH–stretching modes of the methyl groups in resonance with a wide variety of combination bands. This region is again dominated by Fermi resonances, spreading a large number of features over a wide range. No contributions to the 3.51, and 3.56 μm features are predicted for the two methylated PAHs.

The aromatic CH–stretching region is also affected by the inclusion of additional hydrogens or substitution of methyl groups. For the methylated PAHs the typical aromatic CH–stretching bands are pushed to higher energies (up as high as 3100 cm^{-1}), however they also now begin to resonate with lower energy combination bands involving methyl CH–bending modes (down to 3050 cm^{-1}) resulting in a wider, more even distribution of intensity over the aromatic region than a normal PAH. The aromatic CH–stretching region of the hydrogenated PAHs show similar behavior in that the intensity is distributed over a wider range than a normal PAH. However, there is no shift to higher energies, and the intensity is more concentrated in the lower energy aromatic modes and resonances. At higher temperatures, as lines broaden and blend, these behaviors will affect apparent line widths and positions.

It has also been proposed[124] that the feature at 6.9 μm (1450 cm^{-1}) is likely due to HCH–bending modes (or so–called *methylene scissoring* modes) of hydrogenated PAHs, and could be used as a tracer for hydrogenated PAHs in astronomical observations. The HCH–bending modes are indeed stronger around 6.9 μm, but regular in–plane CH–bending modes also gain significant intensity in this region. Complicating matters further, enhancements in intensities in this region are now also observed for the methylated PAHs. For the methylated PAHs this enhanced region extends from 6.9 μm down to 7.4 μm (1450 cm^{-1}) consisting of combination bands of both CC and CH out–of–plane bending modes.

5.5 Conclusions

This work presented the anharmonic spectrum of six CH–bond–containing PAHs: 9–methylanthracene, 9,10–dimethylanthracene, 9,10–dihydroanthracene, 9,10–dihydrophenanthrene, 1,2,3,4–tetrahydronaphthalene, and 1,2,3,6,7,8–hexahydropyrene. The choice of these PAHs was motivated largely by the need to describe accurately the CH–stretching region (3100 – 2800 cm^{-1}) to aid in the analysis of astronomical observations of the AIBs. Particularly, to explain the source of the 3.40, 3.46, 3.51, and 3.56 μm (2941, 2890, 2849, and 2809 cm^{-1}) IR features observed in a variety of astronomical objects. We have shown that hydrogenated PAHs can contribute to the 3.40, 3.46, and 3.51, μm features, and methylated PAHs to the 3.40, 3.46 μm features. No experimental bands were found to explain the 3.56 μm feature. In conjunction with the low–temperature high–resolution gas–phase spectra presented here, the vibrational sources of the dominant features in the CH–stretching region have been identified and characterized. As in our previous work[105, 125] Fermi resonances are shown to dominate the aromatic

CH–stretching region. Without proper treatment of resonances (i.e., polyad treatment) this region cannot be reproduced accurately. Fermi resonances are now shown to not affect only aromatic CH–stretching modes but also aliphatic CH–stretching modes. This results in many more strong aliphatic bands than would be predicted at the harmonic level. The CH–stretching region has been shown to be the most sensitive upon hydrogenation or methylation; with the gradual loss of aromatic features centered around 3050 cm^{-1} and the rise of the aliphatic features around 2900 cm^{-1}. Not only is there a loss in aromatic fundamental features, but the ability for the remaining aromatic fundamentals to engage in resonances is found to diminish as the molecule becomes more aliphatic. Conversely, as the aliphatic fundamental features become stronger their tendency to engage in strong resonances increases.

IR features have also been characterized in conjunction with MIS data for the range of 2000 through 500 cm^{-1}. The changes to the IR spectra of the hydrogenated and methylated PAHs in this region can be attributed mainly to changes in which IR modes are active (i.e., molecular symmetry considerations), or changes to the edge structure (i.e., solo, duo, trio, quarto out–of–plane CH–bending modes). These changes are not unique to hydrogenation or methylation of PAHs, but are seen across various PAH species and derivatives. The only significant changes that correlate with hydrogenation or methylation (save for the CH–stretching region discussed above) are the features between 1450 and 1350 cm^{-1}. The hydrogenated PAHs show a significant enhancement in intensity to the features near 1450 cm^{-1} compared to their non–hydrogenated counterparts. These features are confirmed as being due to CH_2 bending modes. The methylated PAHs also show enhanced features near 1450 cm^{-1}, but these are less localized and extend down to 1350 cm^{-1}. The features here consist of combination bands of both CC and CH out–of–plane bending modes.

Line position agreement between the anharmonic treatment of this work and the low–temperature high–resolution gas–phase is excellent, agreeing with an average deviation of 0.00% ± 0.17%. The MIS line positions agree with an average deviation of -0.07% ± 0.30%, well within expected experimental limitations. As stated previously, the improvement in accuracy compared to our previous work is due to the improved basis/functional combination (B3LYP/N07D) in the anharmonic approach. The issues observed in the previously recommended basis/functional for anharmonic calculations of PAHs (B97-1/TZ2P) lead to the call for a more in–depth benchmark study.

With the current anharmonic analysis of our collection of PAH families, the extensions into temperature dependent spectra, and full emission spectra are both feasible and currently underway.

Acknowledgements

The authors would like to thank Scott Sandford (NASA Ames) for providing the MIS data. The spectroscopic study of interstellar PAHs at Leiden Observatory have been supported through the Advanced European Research Council Grant

246976, a Spinoza award, and through the Dutch Astrochemistry Network funded by the Netherlands Organization for Scientific Research, NWO. We acknowledge the European Union (EU) and Horizon 2020 funding awarded under the Marie Sklodowska–Curie action to the EUROPAH consortium, grant number 722346. Calculations were carried out on the Dutch national e–infrastructure (Cartesius) with the support of SURF Cooperative, under NWO EW project SH-362-15. AC acknowledges NWO for a VENI grant (639.041.543). AP acknowledges NWO for a VIDI grant (723.014.007). XH and TJL gratefully acknowledge support from the NASA 12–APRA12–0107 grant. XH acknowledges the support from NASA/SETI Co–op Agreement NNX15AF45A. This material is based upon work supported by the National Aeronautics and Space Administration through the NASA Astrobiology Institute under Cooperative Agreement Notice NNH13ZDA017C issued through the Science Mission Directorate.

5.6 Supplemental Material

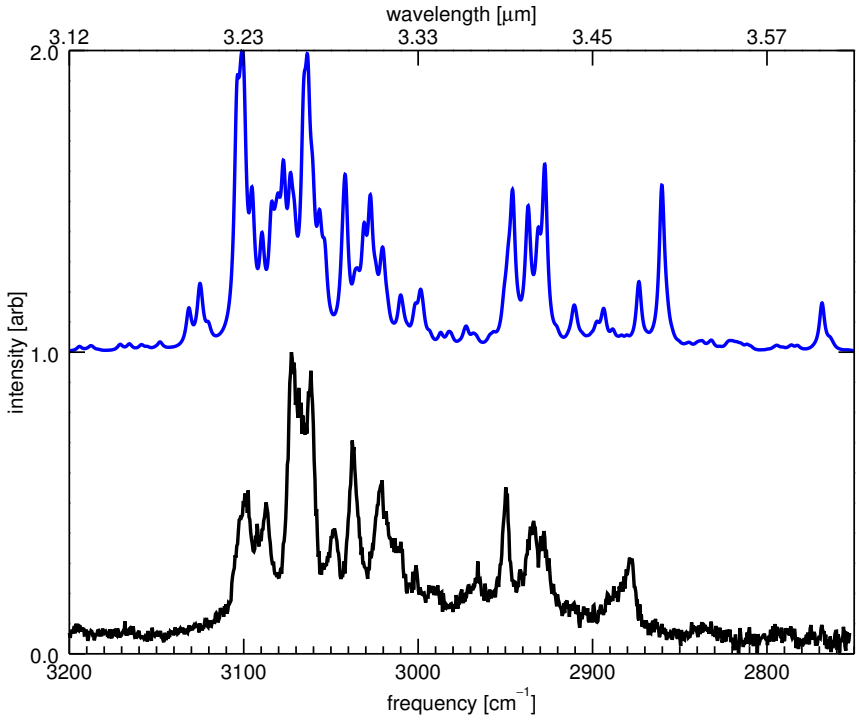

Figure 5.8 Theoretical anharmonic IR spectrum of this work of 9–methylanthracene compared with the high–resolution gas–phase IR absorption spectrum of this work.

exp[27]	rel I[27]	anharm	rel I	components	I source
3099.3	0.53	3100.0	0.58	ν_2, $\nu_{13}+\nu_{22}$, ν_4	ν_2, ν_4
		3101.6	0.42	$\nu_{16}+\nu_{17}$, ν_{13}	ν_3
3092.3	0.43	3089.5	0.40	$\nu_{14}+\nu_{19}$, $\nu_{15}+\nu_{18}$, $\nu_{14}+\nu_{21}$, ν_8	ν_4, ν_1
3087.1	0.50	3083.8	0.50	$\nu_{13}+\nu_{19}$, ν_3	ν_3, ν_1
3072.7	1	3077.3	0.64	$\nu_{13}+\nu_{22}$, $\nu_{14}+\nu_{21}$, ν_1	ν_1, ν_4
3068.5	0.88	3073.1	0.60	$\nu_{14}+\nu_{22}$, $\nu_{14}+\nu_{19}$, $\nu_{13}+\nu_{22}$, ν_4	ν_4
3061.5	0.94	3063.6	0.99	ν_4, $\nu_{14}+\nu_{22}$, ν_5	ν_4, ν_3, ν_5, ν_6
3048.0	0.41	3056.6	0.47	ν_5, $\nu_{14}+\nu_{22}$	ν_5
3037.8	0.70	3041.8	0.26	ν_9, $\nu_{15}+\nu_{19}$, $\nu_{13}+\nu_{23}$, ν_5	ν_5, ν_9
		3041.6	0.32	$\nu_{16}+\nu_{18}$, ν_6	ν_6, ν_4
3020.6	0.58	3027.4	0.52	ν_{10}, $\nu_{15}+\nu_{21}$, $\nu_{15}+\nu_{22}$	ν_{10}
3001.2	0.30	2998.6	0.21	$\nu_{16}+\nu_{22}$, $\nu_{13}+\nu_{26}$	ν_4, ν_3
2965.8	0.30	2972.5	0.09	$\nu_{15}+\nu_{24}$	ν_4, ν_3
2949.8	0.55	2945.9	0.54	ν_{11}, $\nu_{18}+\nu_{20}$	ν_{11}
2933.8	0.44	2936.9	0.49	$\nu_{18}+\nu_{22}$, ν_{12}	ν_{12}
2927.9	0.40	2927.4	0.62	$\nu_{19}+\nu_{19}$, ν_{12}, $\nu_{18}+\nu_{22}$	ν_{12}
2877.5	0.32	2860.3	0.55	$\nu_{20}+\nu_{20}$, ν_{12}	ν_{12}

Table 5.1 Line positions [cm^{-1}], relative intensities, resonance components, and intensity origins for the bands of 9–methylanthracene determined from the high–resolution gas–phase IR absorption spectra and the theoretical anharmonic spectrum of this work (figure 5.8).

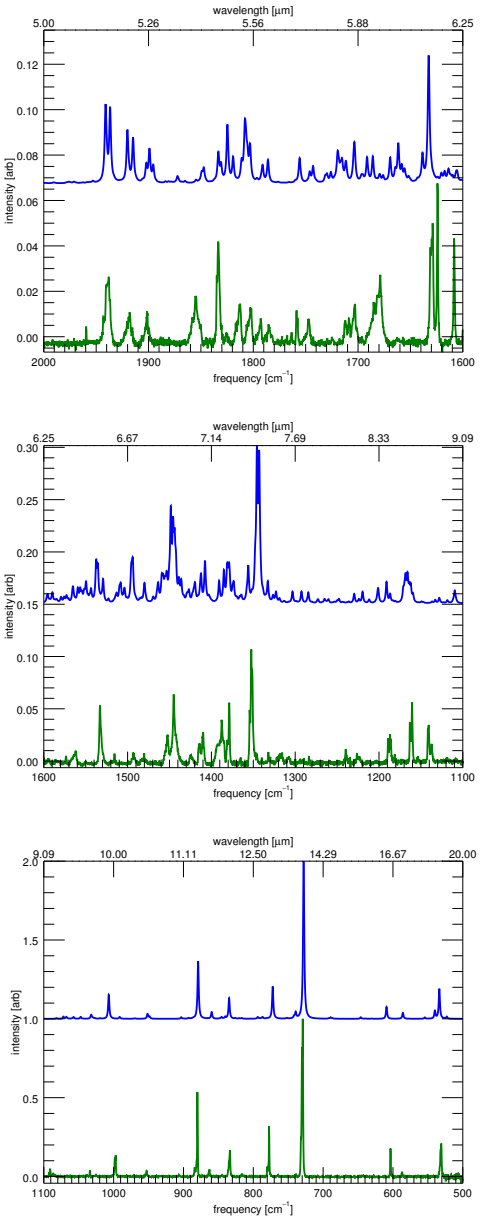

Figure 5.9 The matrix–isolation infrared spectrum[36, 79] of 9–methylanthracene (green, bottom of each panel) compared to the convolved (FWHM 2 cm^{-1}) theoretical anharmonic calculations of this work (blue, top each panel). Three spectral ranges are shown, with each range normalized to the local maximum to enhance details.

exp[36, 79]	rel I	anharm	rel I	mode
1939.1	0.030	1941.0	0.035	$\nu_{42} + \nu_{42}$
1918.8	0.012	1920.2	0.024	$\nu_{44} + \nu_{42}$
1901.5	0.011	1899.1	0.015	$\nu_{45} + \nu_{44}$
1855.0	0.018	1847.3	0.007	$\nu_{47} + \nu_{43}$
1833.4	0.045	1824.7	0.026	$\nu_{42} + \nu_{49}$
1825.7	0.004	1819.3	0.012	$\nu_{43} + \nu_{49}$
1813.5	0.016	1807.9	0.029	$\nu_{46} + \nu_{46}$
1802.4	0.015	1803.2	0.018	$\nu_{45} + \nu_{49}$
1793.3	0.009	1791.1	0.008	$\nu_{45} + \nu_{50}$
1784.9	0.006	1786.0	0.010	$\nu_{44} + \nu_{50}$
1758.4	0.013	1755.8	0.011	$\nu_{47} + \nu_{47}$
1747.2	0.010	1742.9	0.008	$\nu_{43} + \nu_{52}$
1711.9	0.006	1719.4	0.014	$\nu_{48} + \nu_{48}$
1709.8	0.008	1715.4	0.011	$\nu_{47} + \nu_{50}$
1703.3	0.016	1703.5	0.018	$\nu_{44} + \nu_{53}$
1682.7	0.018	1669.3	0.011	$\nu_{37} + \nu_{58}$
1678.8	0.017	1661.6	0.018	$\nu_{45} + \nu_{55}$
1629.7	0.053	1632.7	0.056	ν_{13}
1573.4	0.007	1572.9	0.008	$\nu_{28} + \nu_{70}$
1563.0	0.010	1565.2	0.016	ν_{16}
1532.6	0.052	1537.4	0.042	ν_{17}
1515.6	0.009	1508.3	0.020	$\nu_{51} + \nu_{56}$
1492.9	0.008	1494.0	0.044	ν_{18}
1480.9	0.004	1479.9	0.020	$\nu_{54} + \nu_{54}$
1452.7	0.024	1457.7	0.028	$\nu_{37} + \nu_{66}$
1444.5	0.053	1448.4	0.093	$\nu_{44} + \nu_{63}$
1424.3	0.007	1419.7	0.020	$\nu_{45} + \nu_{64}$
1414.3	0.020	1412.4	0.029	$\nu_{47} + \nu_{61}$
1410.1	0.029	1407.6	0.041	ν_{23}
1388.2	0.023	1390.8	0.022	ν_{24}
1387.6	0.020	1385.1	0.032	ν_{25}
1378.8	0.056	1380.9	0.039	$\nu_{49} + \nu_{61}$
1352.1	0.104	1345.6	0.151	ν_{27}
1332.0	0.011	1332.7	0.021	ν_{28}
1317.5	0.007	1322.9	0.011	$\nu_{54} + \nu_{59}$
1307.9	0.005	1303.2	0.011	$\nu_{52} + \nu_{61}$
1239.5	0.011	1229.6	0.009	ν_{31}
1225.1	0.006	1219.6	0.011	$\nu_{58} + \nu_{58}$
1189.1	0.022	1191.0	0.021	ν_{32}
1186.6	0.026	1186.8	0.009	ν_{33}
1162.9	0.036	1168.3	0.029	$\nu_{52} + \nu_{66}$
1160.6	0.057	1166.0	0.030	ν_{34}
1141.0	0.039	-	-	
1137.3	0.017	-	-	
1090.9	0.049	1109.5	0.012	$\nu_{60} + \nu_{60}$
1086.5	0.017	-	-	
1033.9	0.041	1032.1	0.027	ν_{38}
997.8	0.133	1007.0	0.153	ν_{41}
952.8	0.038	951.5	0.032	ν_{44}
880.0	0.507	879.1	0.363	ν_{47}
863.1	0.041	859.6	0.043	ν_{48}
833.9	0.156	834.6	0.133	ν_{50}
816.1	0.016	816.7	0.006	$\nu_{62} + \nu_{69}$
777.4	0.301	772.2	0.205	ν_{52}
729.7	1	727.9	1	ν_{55}
603.5	0.175	609.2	0.076	ν_{58}
587.0	0.030	585.8	0.038	ν_{59}
531.3	0.217	533.6	0.191	ν_{61}

Table 5.2 Line positions [cm^{-1}], relative intensities, and vibrational mode identifications for the bands of 9–methylanthracene determined from the matrix isolation spectra and the theoretical anharmonic spectrum of this work (figure 5.9).

mode	freq	symm	description
ν_1	3225.9	a′	hindered quarto CH stretch
ν_2	3219.1	a′	unhindered quarto CH stretch
ν_3	3202.1	a′	hindered quarto CH stretch
ν_4	3201.4	a′	unhindered quarto CH stretch
ν_5	3186.9	a′	hindered quarto CH stretch
ν_6	3186.3	a′	unhindered quarto CH stretch
ν_7	3176.8	a′	solo/quarto CH stretch
ν_9	3171.2	a′	solo CH stretch
ν_{10}	3165.6	a′	methyl CH stretch
ν_{11}	3083.7	a″	methyl CH stretch
ν_{12}	3038.6	a′	methyl CH stretch
ν_{13}	1670.9	a′	CC stretch
ν_{14}	1664.2	a′	CC stretch
ν_{15}	1621.0	a′	CC stretch
ν_{16}	1601.1	a′	CC stretch
ν_{17}	1570.8	a′	CC stretch/CH in-plane bend
ν_{18}	1528.1	a′	CH in-plane bend
ν_{19}	1496.6	a′	methyl HCH bend
ν_{20}	1489.7	a″	methyl HCH bend
ν_{21}	1481.9	a′	CH in-plane bend
ν_{22}	1478.0	a′	CH in-plane bend
ν_{23}	1445.3	a′	CC stretch
ν_{24}	1420.1	a′	CH in-plane bend
ν_{25}	1413.1	a′	CH in-plane bend
ν_{26}	1408.6	a′	CH in-plane bend
ν_{27}	1373.8	a′	CH in-plane bend
ν_{28}	1356.7	a′	CH in-plane bend
ν_{31}	1252.0	a′	CH in-plane bend
ν_{32}	1210.4	a′	CH in-plane bend
ν_{33}	1200.7	a′	CH in-plane bend
ν_{34}	1181.4	a′	CH in-plane bend
ν_{37}	1078.8	a′	CH in-plane bend (incl. methyl)
ν_{38}	1050.6	a′	methyl CC stretch
ν_{41}	1025.1	a′	CH in-plane bend (incl. methyl)
ν_{42}	991.2	a″	CH out-of-plane bend
ν_{43}	989.2	a″	CH out-of-plane bend
ν_{44}	971.3	a″	CH out-of-plane bend
ν_{45}	967.3	a″	CH out-of-plane bend
ν_{46}	914.0	a′	CC in-plane bend
ν_{47}	898.6	a″	CH out-of-plane bend
ν_{48}	870.0	a′	CC in-plane bend
ν_{49}	860.2	a″	CH out-of-plane bend
ν_{50}	849.1	a″	CH out-of-plane bend
ν_{51}	830.6	a′	ring breathe
ν_{52}	785.8	a″	CC out-of-plane bend
ν_{53}	765.8	a″	CH out-of-plane bend
ν_{54}	747.2	a″	CH out-of-plane bend
ν_{55}	741.0	a″	CH out-of-plane bend
ν_{56}	698.2	a′	CC in-plane bend
ν_{58}	616.0	a′	CC in-plane bend
ν_{59}	600.8	a″	CC out-of-plane bend
ν_{60}	559.5	a′	CC in-plane bend
ν_{61}	544.8	a″	CC out-of-plane bend
ν_{62}	528.7	a′	CC in-plane bend
ν_{63}	506.8	a″	CC out-of-plane bend
ν_{64}	483.1	a″	CC out-of-plane bend
ν_{66}	405.2	a″	CC out-of-plane bend
ν_{69}	299.5	a″	CC out-of-plane bend
ν_{70}	248.3	a′	body in-plane bend

Table 5.3 Harmonic mode descriptions and frequencies [cm^{-1}] of the IR active modes and modes involved in IR active combination bands for the identifications given in tables 5.1 and 5.2 of 9–methylanthracene.

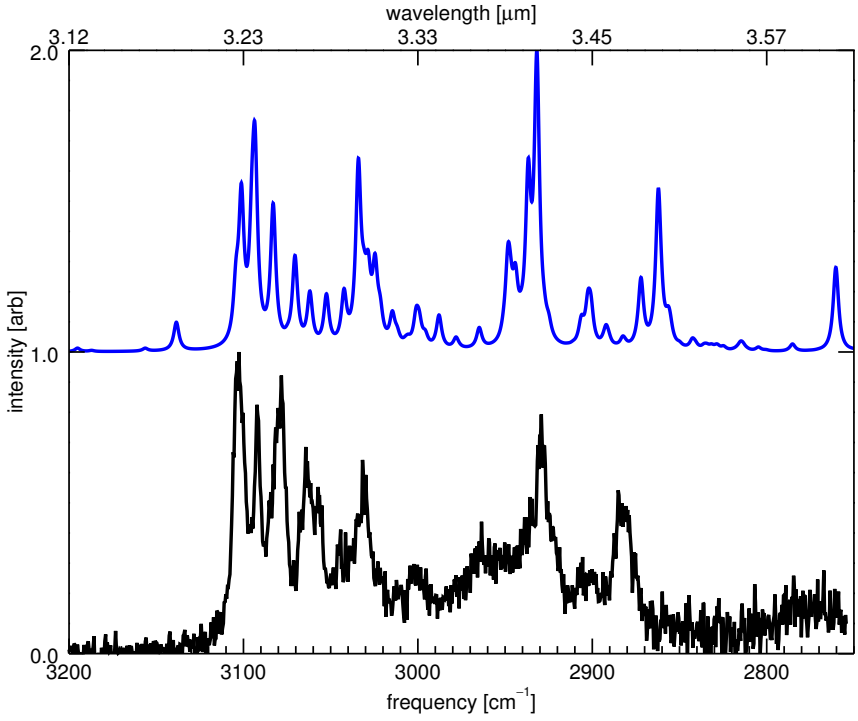

Figure 5.10 Theoretical anharmonic IR spectrum of this work of 9,10–dimethylanthracene compared with the high–resolution gas–phase IR absorption spectrum of this work.

exp[27]	rel I[27]	anharm	rel I	components	I source
3102.6	1	3101.2	0.55	ν_4, $\nu_{16}+\nu_{25}$, $\nu_{16}+\nu_{21}$	ν_4
3092.3	0.83	3093.7	0.77	ν_2, $\nu_{19}+\nu_{20}$	ν_2
3078.3	0.92	3083.0	0.49	$\nu_{16}+\nu_{21}$, ν_4, ν_2	ν_4, ν_2
3063.7	0.47	3070.5	0.32	$\nu_{16}+\nu_{26}$, $\nu_{16}+\nu_{21}$, ν_5	ν_5
3057.3	0.55	3052.4	0.19	$\nu_{16}+\nu_{26}$, $\nu_{19}+\nu_{20}$, ν_5	ν_5
3031.7	0.64	3034.1	0.64	ν_9, $\nu_{15}+\nu_{27}$, $\nu_{18}+\nu_{21}$	ν_9, ν_4
2963.5	0.44	2964.8	0.08	$\nu_{20}+\nu_{21}$	ν_{14}
2929.2	0.79	2932.8	1	ν_{14}, $\nu_{21}+\nu_{24}$	ν_{14}
2885.2	0.54	2862.1	0.54	$\nu_{22}+\nu_{23}$, ν_{14}, $\nu_{21}+\nu_{24}$	ν_{14}

Table 5.4 Line positions [cm^{-1}], relative intensities, resonance components, and intensity origins for the bands of 9,10–dimethylanthracene determined from the high–resolution gas–phase IR absorption spectra and the theoretical anharmonic spectrum of this work (figure 5.10).

mode	freq	symm	description
ν_2	3230.8	b	hindered quatro CH stretch
ν_4	3224.2	b	unhindered quatro CH stretch
ν_5	3196.9	b	CH stretch
ν_9	3168.7	b	methyl hindered CH stretch
ν_{14}	3038.3	b	methyl CH stretch
ν_{15}	1669.4	b	CC stretch
ν_{16}	1657.4	a	CC stretch
ν_{18}	1592.1	a	CC stretch
ν_{19}	1573.3	b	CC stretch
ν_{20}	1536.1	a	CH in-plane bend
ν_{21}	1507.1	b	methyl HCH bend
ν_{22}	1491.0	a	methyl HCH bend
ν_{23}	1490.8	a	methyl HCH bend
ν_{24}	1488.2	a	methyl HCH bend
ν_{25}	1482.5	b	CH in-plane bend
ν_{26}	1474.6	b	CH in-plane bend
ν_{27}	1450.5	a	CC stretch

Table 5.5 Harmonic mode descriptions and frequencies [cm^{-1}] of the IR active modes and modes involved in IR active combination bands for the identifications given in table 5.4 of 9,10–dimethylanthracene.

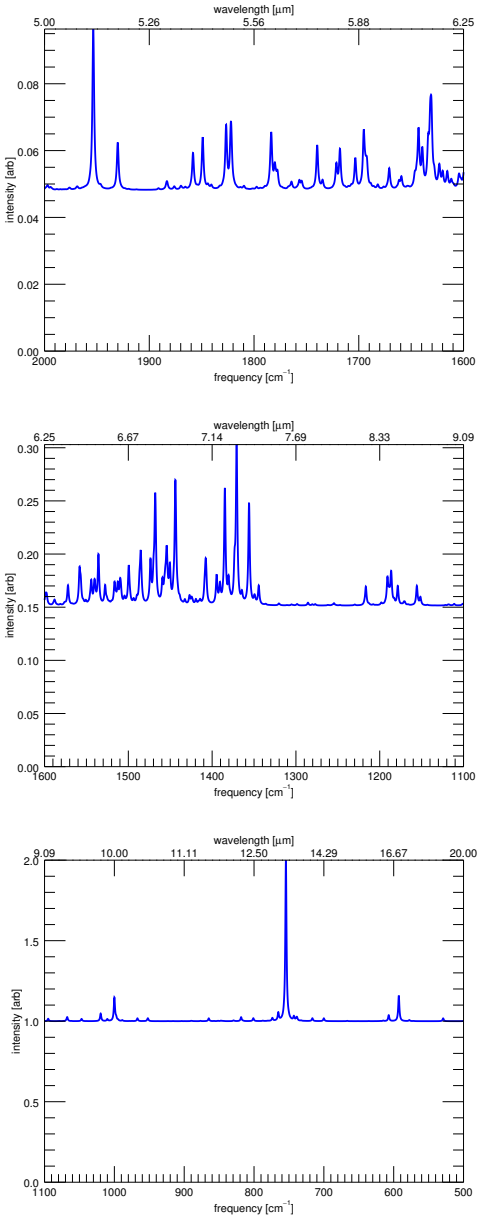

Figure 5.11 No matrix–isolation data is available for 9,10–dimethylanthracene. Therefore, only the convolved (FWHM 2 cm^{-1}) theoretical anharmonic calculations of this work (blue, top each panel). Three spectral ranges are shown, with each range normalized to the local maximum to enhance details.

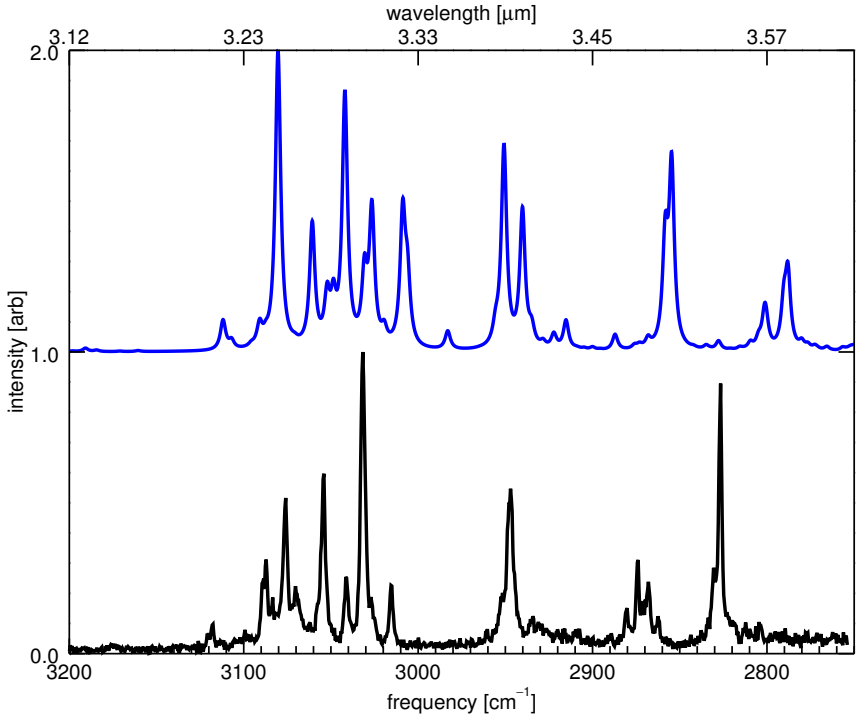

Figure 5.12 Theoretical anharmonic IR spectrum of this work of 9,10–dihydroanthracene compared with the high–resolution gas–phase IR absorption spectrum of this work.

exp[27]	rel I[27]	anharm	rel I	components	I source
3118.1	0.10	3111.8	0.11	$\nu_{13}+\nu_{17}$	ν_7
3087.1	0.31	3090.7	0.11	$\nu_{14}+\nu_{18}$	ν_7
3075.9	0.52	3080.3	1	ν_4, $\nu_{15}+\nu_{19}$, $\nu_{16}+\nu_{20}$	ν_4
3070.3	0.22	3060.7	0.43	$\nu_{16}+\nu_{18}$, ν_5, $\nu_{14}+\nu_{19}$	ν_5
3054.0	0.60	3042.0	0.87	ν_5, $\nu_{13}+\nu_{20}$, $\nu_{14}+\nu_{19}$	ν_5
3041.5	0.25	3030.6	0.33	$\nu_{13}+\nu_{21}$, ν_7, ν_3	ν_7
3031.7	1	3026.4	0.50	ν_8, ν_4, $\nu_{16}+\nu_{20}$	ν_4
3015.5	0.23	3008.7	0.51	ν_7, $\nu_{16}+\nu_{19}$, $\nu_{15}+\nu_{20}$	ν_7
2947.0	0.55	2950.8	0.69	ν_{10}, $\nu_{14}+\nu_{23}$	ν_{10}
2934.2	0.12	2940.2	0.48	ν_{10}, $\nu_{14}+\nu_{23}$, $\nu_{13}+\nu_{25}$	ν_{10}
2880.2	0.15	2887.1	0.06	$\nu_{13}+\nu_{26}$	ν_5
2873.8	0.31	2858.0	0.47	ν_{11}, $\nu_{21}+\nu_{22}$	ν_{11}, ν_{10}
2868.0	0.24	2854.7	0.66	ν_{12}, $\nu_{21}+\nu_{21}$	ν_{12}
2862.6	0.12				
2830.6	0.28	2801.1	0.16	$\nu_{15}+\nu_{29}$, $\nu_{19}+\nu_{24}$	ν_{12}
2826.6	0.90	2788.2	0.30	$\nu_{19}+\nu_{24}$, ν_{12}	ν_{12}

Table 5.6 Line positions [cm^{-1}], relative intensities, resonance components, and intensity origins for the bands of 9,10–dihydroanthracene determined from the high–resolution gas–phase IR absorption spectra and the theoretical anharmonic spectrum of this work (figure 5.12).

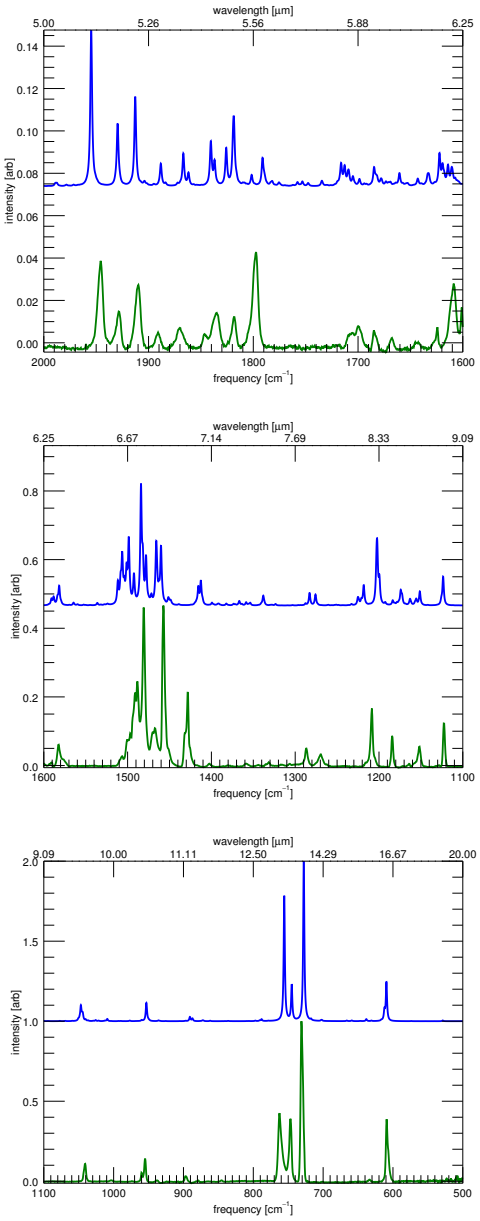

Figure 5.13 The matrix–isolation infrared spectrum[36, 79] of 9,10–dihydroanthracene (green, bottom of each panel) compared to the convolved (FWHM 2 cm^{-1}) theoretical anharmonic calculations of this work (blue, top each panel). Three spectral ranges are shown, with each range normalized to the local maximum to enhance details.

exp[36, 79]	rel I	anharm	rel I	mode
1946.1	0.040	1954.7	0.074	$\nu_{42} + \nu_{41}$
1928.8	0.016	1929.5	0.030	$\nu_{44} + \nu_{41}$
1910.3	0.030	1912.7	0.042	$\nu_{45} + \nu_{42}$
1891.1	0.007	1888.3	0.011	$\nu_{45} + \nu_{44}$
1870.0	0.009	1866.8	0.016	$\nu_{46} + \nu_{41}$
1846.0	0.006	1840.5	0.021	$\nu_{49} + \nu_{41}$
1835.7	0.017	1837.0	0.013	$\nu_{47} + \nu_{44}$
1818.6	0.014	1825.8	0.018	$\nu_{46} + \nu_{45}$
1798.1	0.044	1818.7	0.033	$\nu_{45} + \nu_{48}$
1702.1	0.009	1709.1	0.008	$\nu_{41} + \nu_{55}$
1684.1	0.008	1684.7	0.009	$\nu_{45} + \nu_{52}$
1667.9	0.005	1660.5	0.006	$\nu_{45} + \nu_{54}$
1643.5	0.003	1643.0	0.004	$\nu_{47} + \nu_{52}$
1582.5	0.055	1581.7	0.058	ν_{16}
1507.5	0.025	1511.6	0.074	$\nu_{41} + \nu_{60}$
1499.7	0.069	1506.4	0.158	$\nu_{48} + \nu_{57}$
1489.5	0.228	1498.6	0.201	$\nu_{49} + \nu_{57}$
1480.6	0.418	1484.0	0.356	ν_{18}
1468.9	0.100	1478.0	0.148	$\nu_{53} + \nu_{54}$
1457.3	0.424	1465.8	0.189	$\nu_{43} + \nu_{61}$
1428.8	0.167	1412.6	0.074	ν_{22}
1402.5	0.006	1399.3	0.009	$\nu_{47} + \nu_{61}$
1358.4	0.006	1366.7	0.014	$\nu_{55} + \nu_{57}$
1331.8	0.009	1338.1	0.029	ν_{23}
1286.7	0.048	1282.9	0.037	ν_{26}
1269.8	0.031	1275.8	0.033	ν_{27}
1208.6	0.125	1202.3	0.196	ν_{30}
1184.2	0.089	1174.0	0.046	ν_{33}
1152.0	0.053	1151.3	0.041	ν_{34}
1122.4	0.129	1123.5	0.084	ν_{37}
1041.1	0.110	1046.9	0.101	ν_{39}
959.7	0.050	959.8	0.008	$\nu_{58} + \nu_{66}$
955.0	0.145	953.1	0.115	ν_{44}
937.9	0.006	935.7	0.005	ν_{45}
896.6	0.035	890.8	0.028	ν_{46}
761.6	0.387	755.7	0.784	ν_{52}
747.0	0.382	745.0	0.231	ν_{53}
730.5	1	727.7	1	ν_{54}
633.6	0.011	638.1	0.013	ν_{57}
608.5	0.351	609.3	0.246	ν_{58}

Table 5.7 Line positions [cm^{-1}], relative intensities, and vibrational mode identifications for the bands of 9,10–dihydroanthracene determined from the matrix isolation spectra and the theoretical anharmonic spectrum of this work (figure 5.13).

mode	freq	symm	description
ν_3	3202.6	b_2	quatro CH stretch
ν_4	3202.4	a_2	quatro CH stretch
ν_5	3188.3	a_1	quatro CH stretch
ν_7	3169.1	b_2	quatro CH stretch
ν_8	3168.8	a_2	dihydro CH in-plane stretch
ν_{10}	3077.3	b_2	dihydro CH in-plane stretch
ν_{11}	2984.6	b_2	dihydro CH out-of-plane stretch
ν_{12}	2979.9	a_1	dihydro CH out-of-plane stretch
ν_{13}	1654.8	b_2	CC stretch
ν_{14}	1647.5	a_2	CC stretch
ν_{15}	1633.8	a_1	CC stretch
ν_{16}	1620.0	b_1	CC stretch
ν_{17}	1528.6	a_1	CH in-plane bend
ν_{18}	1514.8	b_1	CH in-plane bend
ν_{19}	1491.9	a_2	CH in-plane bend
ν_{20}	1483.4	b_2	CH in-plane bend
ν_{21}	1471.1	a_1	dihydro HCH bend
ν_{22}	1466.1	b_2	dihydro HCH bend
ν_{23}	1373.6	a_2	CH in-plane bend
ν_{24}	1367.2	b_1	CH in-plane bend
ν_{25}	1351.8	a_1	CC stretch
ν_{26}	1307.2	b_2	CH in-plane bend
ν_{27}	1304.8	b_1	CH in-plane bend
ν_{29}	1234.1	a_1	CH in-plane bend
ν_{30}	1229.5	b_1	CH in-plane bend
ν_{33}	1195.3	b_2	CC in-plane bend
ν_{34}	1184.2	b_1	CH in-plane bend
ν_{37}	1141.1	b_2	CH in-plane bend
ν_{39}	1062.0	b_1	CC in-plane bend
ν_{41}	988.4	b_2	CH out-of-plane bend
ν_{42}	988.3	a_2	CH out-of-plane bend
ν_{43}	975.1	b_2	dihydro out-of-plane twist
ν_{44}	972.5	a_1	CH out-of-plane bend
ν_{45}	951.9	b_1	CH out-of-plane bend
ν_{46}	911.3	a_1	dihydro out-of-plane twist
ν_{47}	896.2	b_2	CH out-of-plane bend
ν_{48}	877.6	a_2	CH out-of-plane bend
ν_{49}	870.0	a_2	CC in-plane bend
ν_{52}	769.0	a_1	CC in-plane bend
ν_{53}	756.9	b_1	CH out-of-plane bend
ν_{54}	739.1	a_1	ring breathe
ν_{55}	726.3	a_2	CC out-of-plane bend
ν_{57}	641.9	b_2	CC out-of-plane bend
ν_{58}	618.8	a_1	CC in-plane bend
ν_{60}	530.9	a_2	CC in-plane bend
ν_{61}	521.2	a_2	CC out-of-plane bend
ν_{66}	359.0	a_1	body drum

Table 5.8 Harmonic mode descriptions and frequencies [cm^{-1}] of the IR active modes and modes involved in IR active combination bands for the identifications given in tables 5.6 and 5.7 of 9,10–dihydroanthracene.

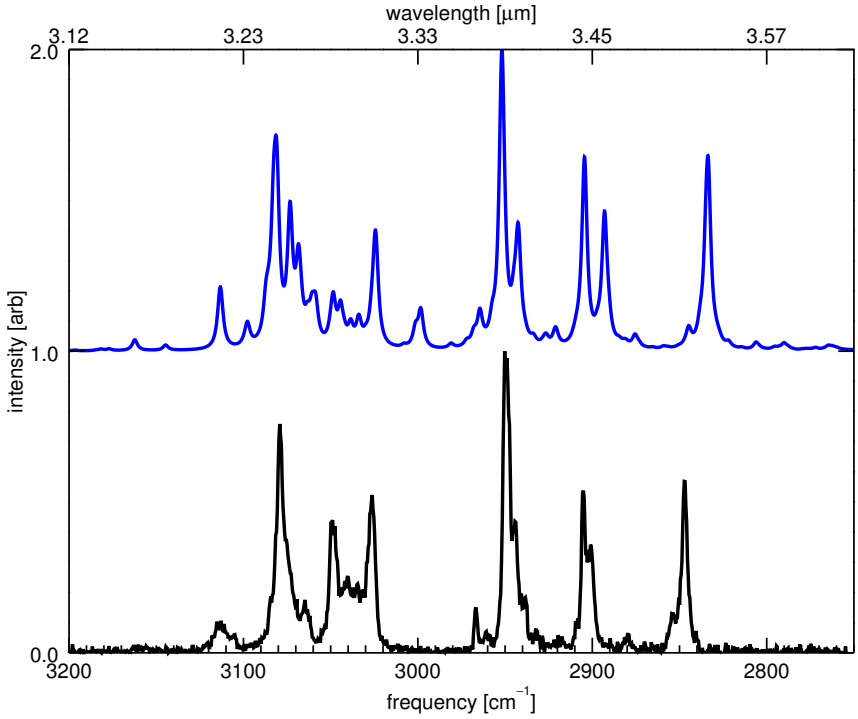

Figure 5.14 Theoretical anharmonic IR spectrum of this work of 9,10–dihydrophenanthrene compared with the high–resolution gas–phase IR absorption spectrum of this work.

exp[27]	rel I[27]	anharm	rel I	components	I source
3112.9	0.10	3113.0	0.11	$\nu_{13}+\nu_{18}$, $\nu_{14}+\nu_{17}$, ν_1	ν_1
		3113.6	0.10	$\nu_{13}+\nu_{17}$, $\nu_{14}+\nu_{18}$, ν_4	ν_4
3079.2	0.76	3081.4	0.72	ν_2, $\nu_{16}+\nu_{18}$, ν_4	ν_2, ν_4
3064.7	0.18	3059.2	0.20	$\nu_{16}+\nu_{17}$, ν_1	ν_1
3048.9	0.44	3048.5	0.20	$\nu_{16}+\nu_{18}$, ν_2	ν_2
3040.1	0.25	3044.4	0.17	$\nu_{14}+\nu_{19}$, $\nu_{14}+\nu_{22}$	ν_4, ν_2
3034.5	0.23	3033.9	0.12	$\nu_{15}+\nu_{19}$, $\nu_{14}+\nu_{21}$, $\nu_{16}+\nu_{21}$, ν_5	ν_5
3026.2	0.52	3024.0	0.22	ν_7, $\nu_{15}+\nu_{22}$, $\nu_{14}+\nu_{21}$	ν_7
		3024.6	0.18	ν_8, $\nu_{13}+\nu_{21}$, ν_4	ν_4, ν_8
2966.7	0.15	2964.4	0.14	$\nu_{13}+\nu_{23}$, $\nu_{18}+\nu_{18}$	ν_9
2950.2	1	2951.8	1	ν_9	ν_9
2944.3	0.44	2942.6	0.43	ν_{10}, $\nu_{13}+\nu_{24}$, $\nu_{14}+\nu_{23}$	ν_{10}
2938.3	0.18	2941.8	0.14	$\nu_{15}+\nu_{23}$, $\nu_{14}+\nu_{24}$	ν_9
2905.1	0.54	2904.5	0.64	ν_{11}, $\nu_{20}+\nu_{22}$, ν_{10}	ν_{11}, ν_{10}
2901.0	0.36	2893.0	0.46	$\nu_{20}+\nu_{20}$, ν_{12}, ν_9	ν_9, ν_{12}
2879.7	0.07	2875.4	0.06	$\nu_{22}+\nu_{22}$, $\nu_{20}+\nu_{20}$	ν_{12}
2854.5	0.13	2845.6	0.07	$\nu_{17}+\nu_{23}$	ν_{11}
2847.2	0.57	2833.7	0.65	ν_{11}, $\nu_{20}+\nu_{22}$, $\nu_{17}+\nu_{23}$	ν_{11}

Table 5.9 Line positions [cm^{-1}], relative intensities, resonance components, and intensity origins for the bands of 9,10–dihydrophenanthrene determined from the high–resolution gas–phase IR absorption spectra and the theoretical anharmonic spectrum of this work (figure 5.14).

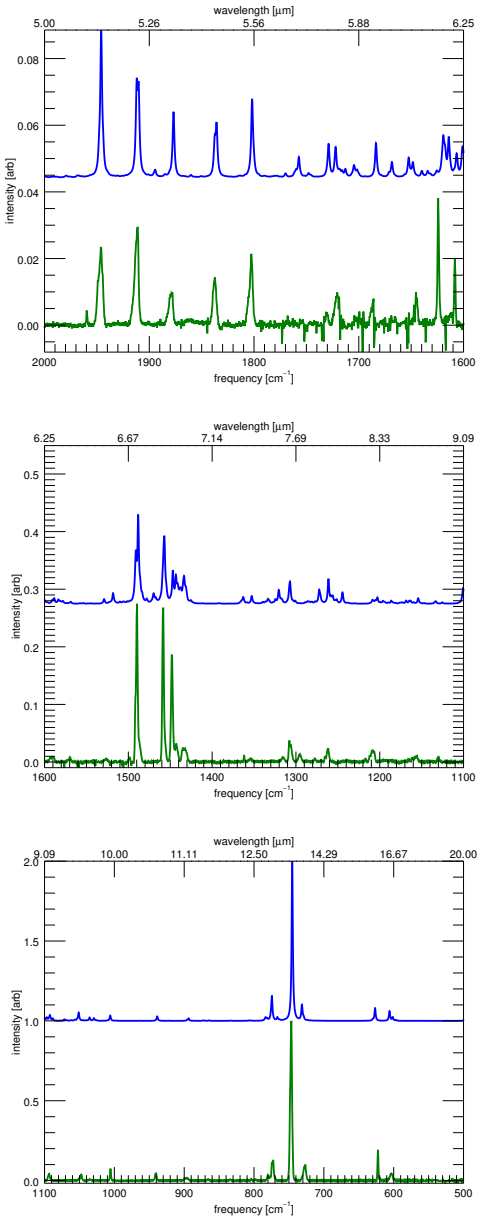

Figure 5.15 The matrix–isolation infrared spectrum[36, 79] of 9,10-dihydrophenanthrene (green, bottom of each panel) compared to the convolved (FWHM 2 cm^{-1}) theoretical anharmonic calculations of this work (blue, top each panel). Three spectral ranges are shown, with each range normalized to the local maximum to enhance details.

exp[36, 79]	rel I	anharm	rel I	mode
1946.6	0.022	1945.9	0.044	$\nu_{44} + \nu_{43}$
1912.1	0.029	1910.3	0.029	$\nu_{45} + \nu_{44}$
1879.4	0.010	1876.8	0.020	$\nu_{46} + \nu_{45}$
1837.7	0.015	1835.8	0.017	$\nu_{48} + \nu_{44}$
1802.9	0.019	1801.8	0.024	$\nu_{48} + \nu_{46}$
1730.5	0.004	1728.8	0.010	$\nu_{49} + \nu_{48}$
1721.0	0.010	1722.1	0.009	$\nu_{51} + \nu_{46}$
1687.4	0.006	1683.6	0.010	$\nu_{54} + \nu_{45}$
1645.1	0.008	1648.3	0.005	$\nu_{51} + \nu_{49}$
1593.0	0.007	1590.5	0.007	$\nu_{37} + \nu_{61}$
1589.6	0.008	1588.5	0.010	ν_{15}
1569.9	0.007	1568.7	0.004	ν_{16}
1489.9	0.253	1488.2	0.154	ν_{18}
1458.5	0.276	1457.1	0.118	ν_{19}
1448.0	0.190	1446.9	0.058	ν_{21}
1443.1	0.030	1443.2	0.050	ν_{20}
1433.3	0.025	1433.5	0.049	ν_{22}
1361.9	0.012	1362.9	0.012	$\nu_{49} + \nu_{61}$
1354.4	0.005	1352.8	0.014	ν_{23}
1315.6	0.008	1320.5	0.024	$\nu_{38} + \nu_{68}$
1306.9	0.034	1307.1	0.039	ν_{26}
1295.4	0.013	-		
1277.4	0.006	1272.2	0.025	$\nu_{52} + \nu_{61}$
1262.0	0.022	1261.2	0.043	ν_{29}
1239.5	0.002	1244.4	0.020	$\nu_{51} + \nu_{62}$
1216.8	0.006	1208.6	0.007	$\nu_{53} + \nu_{63}$
1208.5	0.020	1202.8	0.011	ν_{30}
1165.4	0.004	1168.5	0.006	ν_{34}
1161.0	0.007	1163.3	0.006	$\nu_{52} + \nu_{66}$
1156.4	0.010	1154.1	0.010	ν_{35}
1130.1	0.008	1133.1	0.005	ν_{36}
1093.7	0.042	1092.3	0.037	ν_{37}
1047.5	0.038	1051.1	0.053	ν_{39}
1005.5	0.075	1005.9	0.034	ν_{41}
940.7	0.049	938.7	0.028	ν_{46}
896.9	0.017	893.7	0.016	ν_{47}
779.7	0.032	783.5	0.024	ν_{51}
773.3	0.132	774.4	0.156	ν_{52}
746.9	1	745.3	1	ν_{53}
727.4	0.095	731.4	0.102	ν_{55}
622.5	0.203	626.7	0.080	ν_{57}
603.5	0.044	606.0	0.062	ν_{58}

Table 5.10 Line positions [cm^{-1}], relative intensities, and vibrational mode identifications for the bands of 9,10–dihydrophenanthrene determined from the matrix isolation spectra and the theoretical anharmonic spectrum of this work (figure 5.15).

mode	freq	symm	description
ν_1	3208.4	a	quatro CH stretch
ν_2	3204.5	b	quatro CH stretch
ν_4	3193.8	b	quatro CH stretch
ν_5	3184.3	a	quatro CH stretch
ν_8	3170.5	b	quatro CH stretch
ν_9	3078.5	b	dihydro CH in-plane stretch
ν_{10}	3078.1	a	dihydro CH in-plane stretch
ν_{11}	3013.2	b	dihydro CH out-of-plane stretch
ν_{12}	3003.4	a	dihydro CH out-of-plane stretch
ν_{13}	1652.2	b	CC stretch
ν_{14}	1643.8	a	CC stretch
ν_{15}	1628.2	b	CC stretch
ν_{16}	1607.2	a	CC stretch
ν_{17}	1525.5	a	CH in-plane bend
ν_{18}	1519.1	b	CH in-plane bend
ν_{19}	1486.2	b	CH in-plane bend
ν_{20}	1481.6	a	dihydro HCH bend
ν_{21}	1472.8	b	dihydro HCH bend
ν_{22}	1472.6	a	CH in-plane bend
ν_{23}	1380.9	b	dihydro CH in-plane bend
ν_{24}	1369.1	a	CH in-plane bend
ν_{26}	1339.0	a	dihydro CH in-plane bend
ν_{29}	1282.1	a	CH in-plane bend
ν_{30}	1224.5	a	CH in-plane bend
ν_{34}	1182.1	b	quatro CH in-plane bend
ν_{35}	1178.0	b	dihydro CH in-plane bend
ν_{36}	1149.5	b	CH in-plane bend
ν_{37}	1110.2	a	CC in-plane bend
ν_{38}	1071.8	a	CC in-plane bend
ν_{39}	1068.8	b	CC in-plane bend
ν_{41}	1020.3	b	CC in-plane bend
ν_{43}	989.9	b	dihydro CC in-plane stretch
ν_{44}	988.1	a	CH out-of-plane bend
ν_{45}	955.7	a	CH out-of-plane bend
ν_{46}	955.6	b	CH out-of-plane bend
ν_{47}	908.0	b	dihydro out-of-plane twist
ν_{48}	879.7	b	CH out-of-plane bend
ν_{49}	878.8	a	CH out-of-plane bend
ν_{51}	791.8	a	CH out-of-plane bend
ν_{52}	782.7	b	CH out-of-plane bend
ν_{53}	757.1	b	CH out-of-plane bend
ν_{54}	737.0	a	CH out-of-plane bend
ν_{55}	734.7	b	CC out-of-plane bend
ν_{57}	633.1	b	CC in-plane bend
ν_{58}	610.0	b	CC out-of-plane bend
ν_{61}	503.7	b	CC out-of-plane bend
ν_{62}	470.5	a	CC out-of-plane bend
ν_{63}	466.6	b	CC out-of-plane bend
ν_{66}	392.1	a	body in-plane stretch
ν_{68}	268.2	a	body twist

Table 5.11 Harmonic mode descriptions and frequencies [cm^{-1}] of the IR active modes and modes involved in IR active combination bands for the identifications given in tables 5.9 and 5.10 of 9,10–dihydrophenanthrene.

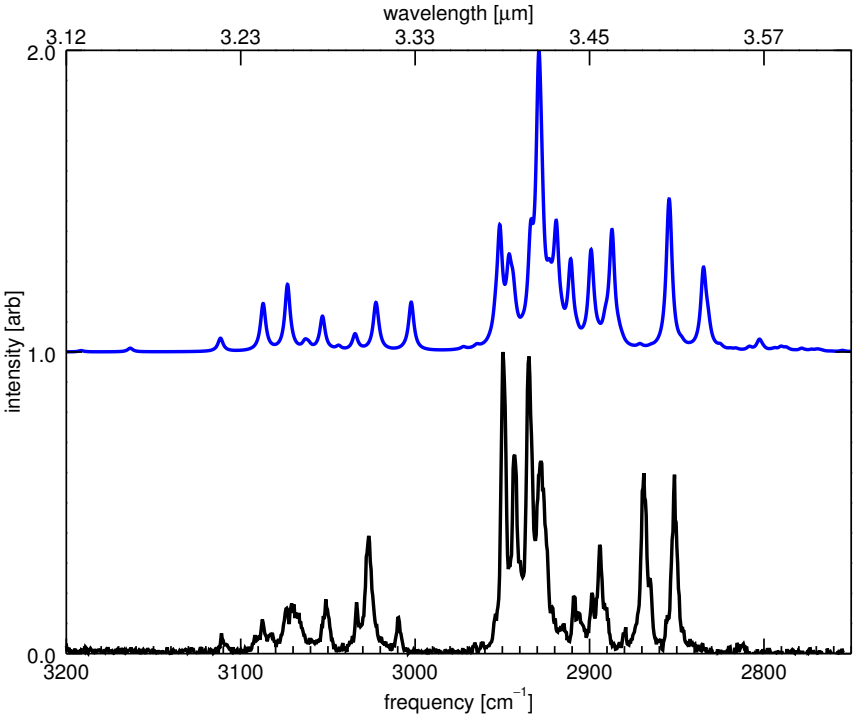

Figure 5.16 Theoretical anharmonic IR spectrum of this work of 1,2,3,4–tetrahydronaphthalene compared with the high–resolution gas–phase IR absorption spectrum of this work.

exp[27]	rel I[27]	anharm	rel I	components	I source
3111.0	0.07	3111.6	0.05	$\nu_{13}+\nu_{15}$, ν_4	ν_4
3087.6	0.10	3087.3	0.16	ν_1, $\nu_{14}+\nu_{15}$, $\nu_{13}+\nu_{18}$	ν_1
3082.5	0.07				
3073.6	0.15	3073.2	0.22	ν_2, $\nu_{14}+\nu_{18}$	ν_2
3070.8	0.17				
3051.2	0.18	3053.1	0.12	ν_3, ν_1, $\nu_{13}+\nu_{18}$	ν_1
3033.6	0.17	3034.4	0.06	ν_3, $\nu_{13}+\nu_{18}$, ν_1	ν_1
3026.6	0.39	3022.5	0.16	$\nu_{14}+\nu_{18}$, ν_4, ν_2	ν_4, ν_2
3009.5	0.12	3003.2	0.16	ν_4, $\nu_{14}+\nu_{18}$, ν_2	ν_4, ν_2
2949.8	1	2951.5	0.42	ν_6, $\nu_{16}+\nu_{16}$, $\nu_{17}+\nu_{17}$, ν_{10}	ν_6, ν_{10}
2942.9	0.66	2946.1	0.33	$\nu_{15}+\nu_{17}$, $\nu_{16}+\nu_{17}$, ν_9	ν_9, ν_8
2934.7	0.99	2929.0	1	ν_5	ν_5
2927.9	0.64	2919.1	0.44	$\nu_{16}+\nu_{16}$, ν_6	ν_6
2909.2	0.19	2910.8	0.31	$\nu_{17}+\nu_{17}$, ν_6, ν_{10}	ν_6, ν_{10}
2898.8	0.20	2899.1	0.34	$\nu_{16}+\nu_{19}$, ν_8	ν_8, ν_{12}
2894.2	0.36	2887.1	0.41	$\nu_{19}+\nu_{20}$, ν_{12}, ν_8, $\nu_{16}+\nu_{19}$	ν_{12}, ν_8
2879.3	0.09	2871.1	0.03	$\nu_{20}+\nu_{20}$, $\nu_{19}+\nu_{19}$	ν_{10}, ν_{11}
2868.9	0.60	2855.4	0.51	ν_{10}, $\nu_{17}+\nu_{17}$, $\nu_{16}+\nu_{20}$	ν_{10}
2851.3	0.60	2834.6	0.28	ν_{12}, $\nu_{19}+\nu_{20}$	ν_{12}

Table 5.12 Line positions [cm^{-1}], relative intensities, resonance components, and intensity origins for the bands of 1,2,3,4–tetrahydronaphthalene determined from the high–resolution gas–phase IR absorption spectra and the theoretical anharmonic spectrum of this work (figure 5.16).

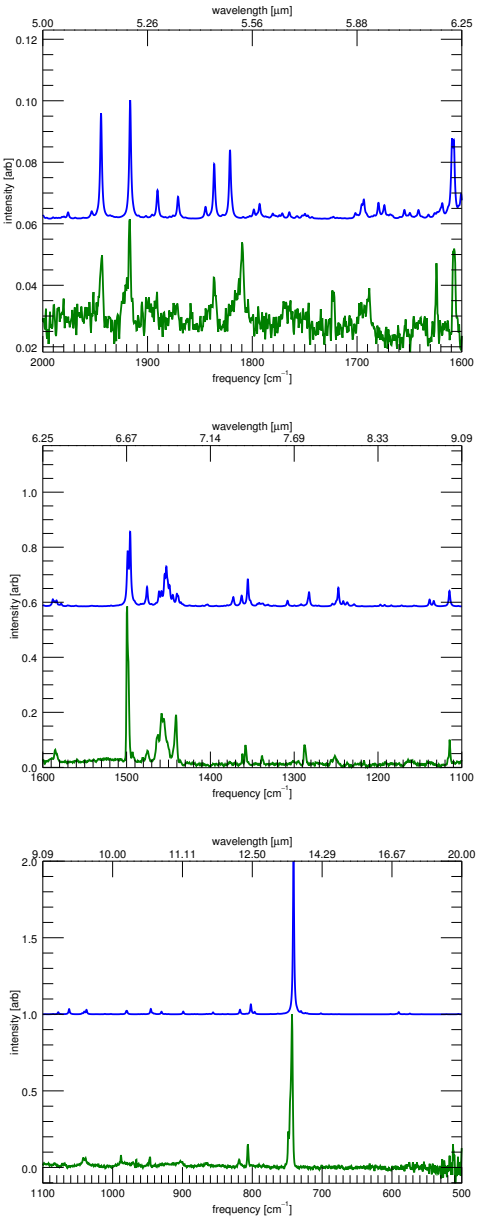

Figure 5.17 The matrix–isolation infrared spectrum[36, 79] of 1,2,3,4–tetrahydronaphthalene (green, bottom of each panel) compared to the convolved (FWHM 2 cm^{-1}) theoretical anharmonic calculations of this work (blue, top each panel). Three spectral ranges are shown, with each range normalized to the local maximum to enhance details.

exp[36, 79]	rel I	anharm	rel I	mode
1944.2	0.024	1944.4	0.034	$\nu_{39} + \nu_{39}$
1916.6	0.030	1916.6	0.039	$\nu_{40} + \nu_{39}$
1896.5	0.005	1890.5	0.009	$\nu_{40} + \nu_{40}$
1836.4	0.015	1837.4	0.011	$\nu_{27} + \nu_{30}$
1810.7	0.021	1821.3	0.023	$\nu_{40} + \nu_{43}$
1692.0	0.012	1693.5	0.006	$\nu_{43} + \nu_{45}$
1589.4	0.012	1588.0	0.026	ν_{14}
1585.2	0.043	1583.6	0.022	$\nu_{35} + \nu_{52}$
1498.9	0.624	1495.8	0.272	ν_{15}
1475.3	0.046	1475.6	0.071	$\nu_{39} + \nu_{52}$
1457.2	0.186	1452.6	0.146	ν_{17}
1441.4	0.196	1440.0	0.046	ν_{19}
1357.9	0.086	1355.3	0.100	ν_{21}
1338.1	0.036	1341.7	0.013	ν_{22}
1287.3	0.090	1282.3	0.052	ν_{26}
1251.9	0.034	1247.3	0.068	ν_{27}
1114.5	0.088	1114.7	0.057	ν_{34}
1040.1	0.048	1037.4	0.030	ν_{37}
988.0	0.063	979.7	0.023	ν_{38}
946.8	0.072	945.3	0.035	ν_{40}
860.7	0.019	856.2	0.013	ν_{44}
818.5	0.047	817.6	0.030	ν_{45}
806.3	0.174	802.1	0.065	ν_{46}
743.7	1	741.0	1	ν_{47}

Table 5.13 Line positions [cm^{-1}], relative intensities, and vibrational mode identifications for the bands of 1,2,3,4–tetrahydronaphthalene determined from the matrix isolation spectra and the theoretical anharmonic spectrum of this work (figure 5.17).

mode	freq	symm	description
ν_1	3200.2	a	quatro CH stretch
ν_2	3185.1	b	quatro CH stretch
ν_3	3165.7	a	quatro CH stretch
ν_4	3162.4	b	quatro CH stretch
ν_5	3073.0	b	dihydro CH stretch
ν_6	3070.0	a	dihydro CH stretch
ν_8	3057.9	b	dihydro CH stretch
ν_9	3025.4	b	dihydro CH stretch
ν_{10}	3020.3	a	dihydro CH stretch
ν_{11}	3006.9	a	dihydro CH stretch
ν_{12}	3006.4	b	dihydro CH stretch
ν_{13}	1649.3	b	aromatic CC stretch
ν_{14}	1622.1	a	aromatic CC stretch
ν_{15}	1525.4	a	aromatic CH in-plane bend
ν_{16}	1502.0	a	dihydro HCH bend
ν_{17}	1492.5	b	dihydro HCH bend
ν_{18}	1482.2	b	aromatic CH in-plane bend/dihydro HCH bend
ν_{19}	1478.8	b	aromatic CH in-plane bend/dihydro HCH bend
ν_{20}	1473.8	a	dihydro HCH bend
ν_{21}	1387.2	a	dihydro CH in-plane bend
ν_{22}	1373.8	a	dihydro CH in-plane bend
ν_{26}	1310.2	b	CH in-plane bend
ν_{27}	1272.9	a	dihydro CH in-plane bend
ν_{30}	1200.8	b	aromatic CC in-plane bend
ν_{34}	1134.3	b	quatro CH in-plane bend
ν_{35}	1100.5	a	alaphatic CC out-of-plane bend
ν_{37}	1056.1	a	ring breathe
ν_{38}	995.3	b	CC in-plane bend
ν_{39}	988.3	a	quatro CH out-of-plane bend
ν_{40}	961.5	b	quatro CH out-of-plane bend
ν_{43}	880.5	a	CH out-of-plane bend
ν_{44}	872.7	a	alaphatic CC in-plane stretch
ν_{45}	829.4	a	alaphatic CC out-of-plane bend
ν_{46}	811.9	b	CC in-plane bend
ν_{47}	753.6	b	quatro CH out-of-plane bend
ν_{52}	512.6	a	CH out-of-plane bend

Table 5.14 Harmonic mode descriptions and frequencies [cm^{-1}] of the IR active modes and modes involved in IR active combination bands for the identifications given in tables 5.12 and 5.13 of 1,2,3,4–tetrahydronaphthalene.

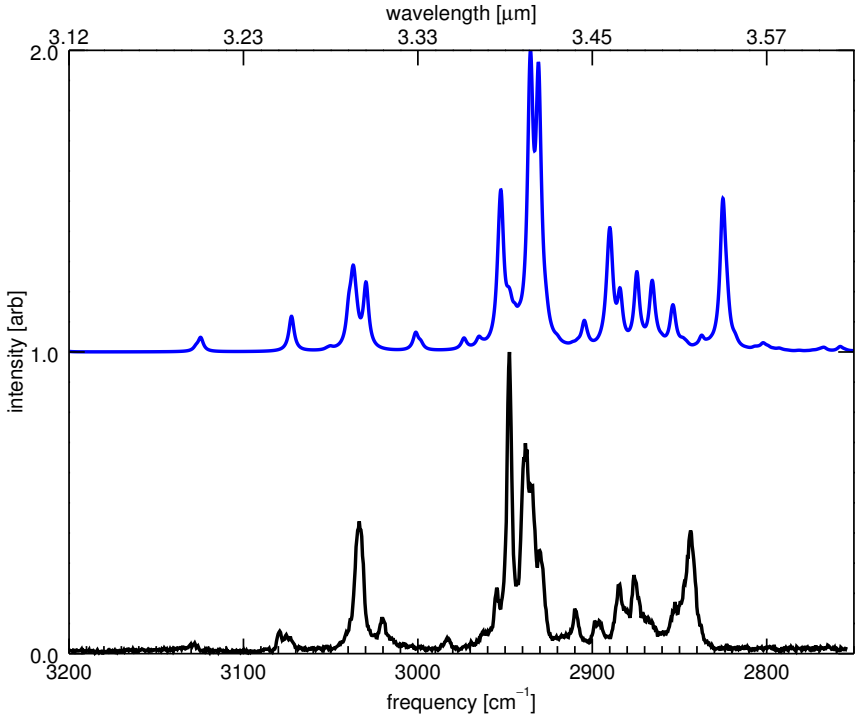

Figure 5.18 Theoretical anharmonic IR spectrum of this work of 1,2,3,6,7,8–hexahydropyrene compared with the high–resolution gas–phase IR absorption spectrum of this work.

exp[27]	rel I[27]	anharm	rel I	components	I source
3128.0	0.04	3124.6	0.05	$\nu_{17}+\nu_{29}$	ν_2
3079.2	0.07				
3075.5	0.06	3072.4	0.12	$\nu_{19}+\nu_{23}$, ν_2	ν_2
3033.6	0.44	3037.1	0.29	$\nu_{17}+\nu_{26}$, ν_2	ν_2
3020.6	0.12	3029.8	0.23	$\nu_{19}+\nu_{27}$, ν_2	ν_2
2982.3	0.05	3001.2	0.07	$\nu_{18}+\nu_{29}$	ν_2
2954.8	0.22				
2947.5	1	2952.4	0.54	$\nu_{21}+\nu_{22}$, ν_8, ν_{12}	ν_8, ν_{12}, ν_6
2938.3	0.70	2935.1	0.47	ν_9, $\nu_{19}+\nu_{33}$	ν_9
		2935.8	0.40	ν_8, ν_6	ν_8, ν_6
		2936.0	0.13	$\nu_{18}+\nu_{35}$, ν_7, $\nu_{19}+\nu_{32}$	ν_7, ν_5, ν_{11}
2934.7	0.56	2931.0	0.96	ν_5	ν_5, ν_{11}
2930.1	0.34	2930.7	-	ν_6	ν_6
2910.1	0.15	2904.6	0.10	$\nu_{21}+\nu_{24}$, $\nu_{21}+\nu_{22}$, $\nu_{22}+\nu_{25}$	ν_8
2896.0	0.10	2890.0	0.41	$\nu_{21}+\nu_{26}$, ν_9	ν_9
2884.3	0.20	2884.2	0.21	$\nu_{24}+\nu_{27}$, $\nu_{25}+\nu_{26}$, ν_{16}, ν_9	ν_9, ν_{16}
2876.1	0.26	2875.4	0.27	$\nu_{26}+\nu_{26}$, $\nu_{27}+\nu_{27}$, ν_{13}	ν_{13}
				$\nu_{26}+\nu_{27}$, ν_{14}	ν_{14}
2852.7	0.17	2853.8	0.16	$\nu_{22}+\nu_{29}$, $\nu_{20}+\nu_{34}$, ν_{11}	ν_{11}
2843.7	0.40	2825.1	0.51	ν_{14}, $\nu_{26}+\nu_{27}$	ν_{14}
				ν_{13}, $\nu_{18}+\nu_{42}$	ν_{13}

Table 5.15 Line positions [cm^{-1}], relative intensities, resonance components, and intensity origins for the bands of 1,2,3,6,7,8–hexahydropyrene determined from the high–resolution gas–phase IR absorption spectra and the theoretical anharmonic spectrum of this work (figure 5.18).

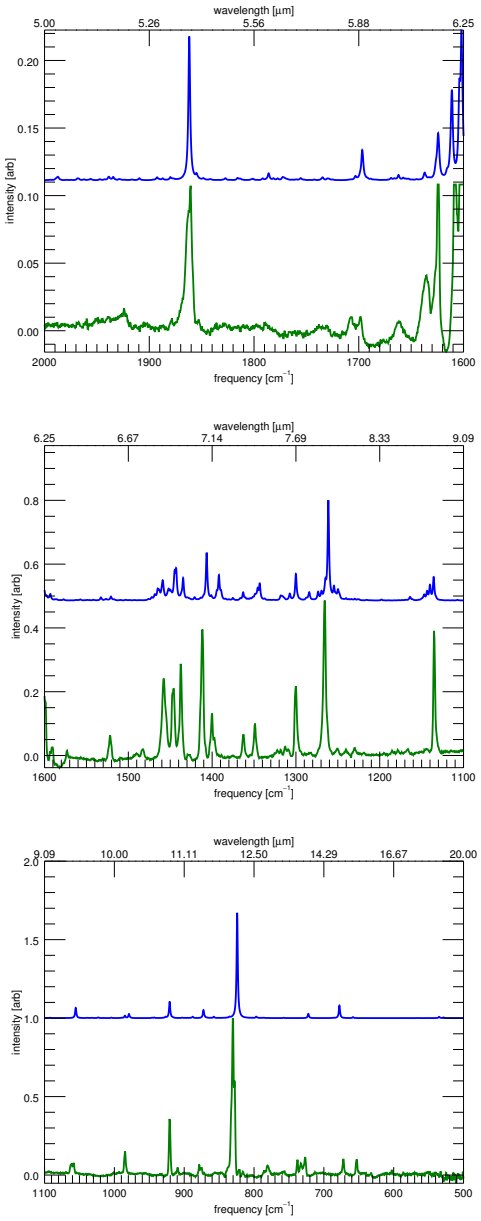

Figure 5.19 The matrix–isolation infrared spectrum[36, 79] of 1,2,3,6,7,8–hexahydropyrene (green, bottom of each panel) compared to the convolved (FWHM 2 cm^{-1}) theoretical anharmonic calculations of this work (blue, top each panel). Three spectral ranges are shown, with each range normalized to the local maximum to enhance details.

exp[36, 79]	rel I	anharm	rel I	mode
1862.1	0.110	1861.8	0.106	$\nu_{57} + \nu_{56}$
1706.4	0.018	1703.1	0.003	$\nu_{57} + \nu_{66}$
1698.2	0.015	1696.7	0.022	$\nu_{62} + \nu_{64}$
1660.7	0.019	1662.1	0.004	$\nu_{64} + \nu_{67}$
1636.0	0.060	1637.1	0.006	$\nu_{56} + \nu_{69}$
1521.8	0.078	1520.7	0.013	ν_{20}
1482.9	0.032	-		
1457.5	0.260	1459.0	0.064	ν_{22}
1446.4	0.249	1444.6	0.096	$\nu_{31} + \nu_{89}$
1437.3	0.310	1434.6	0.071	ν_{26}
1411.8	0.446	1406.6	0.150	ν_{29}
1399.9	0.123	1391.9	0.080	$\nu_{65} + \nu_{72}$
1362.7	0.076	1363.0	0.026	ν_{30}
1348.9	0.105	1345.6	0.054	ν_{32}
1322.2	0.015	1318.1	0.016	$\nu_{58} + \nu_{81}$
1311.6	0.024	1307.3	0.022	$\nu_{55} + \nu_{83}$
1300.1	0.246	1300.1	0.084	ν_{37}
1265.8	0.517	1261.3	0.315	ν_{38}
1250.9	0.020	1254.6	0.047	$\nu_{49} + \nu_{88}$
1240.3	0.015	1249.8	0.036	$\nu_{44} + \nu_{90}$
1229.9	0.021	-		
1135.0	0.419	1135.6	0.074	ν_{48}
1060.2	0.077	1055.4	0.066	ν_{52}
984.8	0.157	979.1	0.026	ν_{55}
920.8	0.406	920.9	0.103	ν_{58}
909.4	0.044	-		
877.0	0.052	872.4	0.051	ν_{61}
830.1	1	824.1	0.671	ν_{64}
780.5	0.058	-		
731.1	0.068	722.2	0.027	ν_{68}
672.1	0.104	677.7	0.080	ν_{70}
653.1	0.114	658.3	0.006	$\nu_{74} + \nu_{88}$

Table 5.16 Line positions [cm^{-1}], relative intensities, and vibrational mode identifications for the bands of 1,2,3,6,7,8–hexahydropyrene determined from the matrix isolation spectra and the theoretical anharmonic spectrum of this work (figure 5.19).

mode	freq	symm	description
ν_2	3177.8	b_1	duo CH stretch
ν_4	3161.5	b_2	duo CH stretch
ν_5	3077.5	a_1	dihydro CH stretch
ν_6	3077.3	b_2	dihydro CH stretch
ν_7	3068.3	b_2	dihydro CH stretch
ν_8	3067.9	b_2	dihydro CH stretch
ν_9	3065.9	b_1	dihydro CH stretch
ν_{11}	3032.8	a_1	dihydro CH stretch
ν_{12}	3032.7	b_2	dihydro CH stretch
ν_{13}	3000.9	a_1	dihydro CH stretch
ν_{14}	3000.8	b_2	dihydro CH stretch
ν_{16}	2998.9	b_1	dihydro CH stretch
ν_{17}	1644.0	a_2	aromatic CC stretch
ν_{18}	1643.7	a_1	aromatic CC stretch
ν_{19}	1638.8	b_2	aromatic CC stretch
ν_{20}	1557.9	b_1	aromatic CC stretch
ν_{21}	1496.4	a_1	dihydro HCH bend
ν_{22}	1496.3	b_2	dihydro HCH bend
ν_{23}	1495.6	a_2	CH in-plane bend
ν_{24}	1485.8	b_2	dihydro HCH bend
ν_{25}	1484.7	a_1	dihydro HCH bend
ν_{26}	1473.4	b_1	dihydro HCH bend
ν_{27}	1471.3	a_2	dihydro HCH bend
ν_{29}	1430.2	b_2	dihydro CH in-plane bend
ν_{30}	1392.4	b_1	duo CH in-plane bend
ν_{31}	1386.4	a_1	CC in-plane stretch
ν_{32}	1376.7	b_2	CH in-plane bend
ν_{33}	1372.3	a_2	dihydro CH in-plane bend
ν_{37}	1331.3	b_1	dihydro CH in-plane bend
ν_{38}	1288.2	b_2	CH in-plane bend
ν_{42}	1249.1	b_2	CH in-plane bend
ν_{44}	1195.4	b_1	dihydro CH in-plane bend
ν_{48}	1156.2	b_1	CH in-plane bend
ν_{49}	1150.0	a_2	CC in-plane bend
ν_{52}	1076.1	b_2	alaphatic CC out-of-plane bend
ν_{55}	995.4	b_2	alaphatic CC in-plane bend
ν_{56}	949.6	b_2	duo CH out-of-plane bend
ν_{57}	947.5	a_2	duo CH out-of-plane bend
ν_{58}	935.4	b_1	CC in-plane bend
ν_{61}	886.6	a_1	dihydro CH out-of-plane bend
ν_{62}	883.4	b_1	CH out-of-plane bend
ν_{64}	841.0	a_1	dihydro CH out-of-plane bend
ν_{65}	832.3	b_2	CC in-plane bend
ν_{66}	812.4	b_1	CH out-of-plane bend
ν_{67}	808.5	b_2	CC out-of-plane bend
ν_{68}	730.6	b_2	CC in-plane bend
ν_{69}	714.5	a_2	CC in-plane bend
ν_{70}	686.4	a_1	CC out-of-plane bend
ν_{72}	586.4	a_1	body breathe
ν_{74}	543.3	b_1	CC in-plane bend
ν_{81}	399.7	a_1	body stretch
ν_{83}	332.9	a_2	CC out-of-plane bend
ν_{88}	131.2	b_1	body twist
ν_{89}	97.7	a_1	out-of plane body bend
ν_{90}	86.9	a_2	body twist

Table 5.17 Harmonic mode descriptions and frequencies [cm^{-1}] of the IR active modes and modes involved in IR active combination bands for the identifications given in tables 5.15 and 5.16 of 1,2,3,6,7,8–hexahydropyrene.